An Interbacterial Cysteine Protease Toxin Inhibits Cell Growth by Targeting Type II DNA Topoisomerases GyrB and ParE

Pin-Yi Song[1,2,6], Chia-En Tsai[1,2,6], Yung-Chih Chen[2], Po-Pang Chen[2,3], Tzu-Haw Wang[4], Chao-Yuan Hu[2], Po-Yin Chen[1,2], Chuan Ku[4,5], Kuo-Chiang Hsia[1,2,3], See-Yeun Ting[1,2,5,7†]

[1] Molecular and Cell Biology, Taiwan International Graduate Program, Academia Sinica and National Defense Medical Center, Taipei, 11490, Taiwan

[2] Institute of Molecular Biology, Academia Sinica, Taipei 11529, Taiwan

[3] Institute of Biochemistry and Molecular Biology, College of Life Sciences, National Yang Ming Chiao Tung University, Taipei 11221, Taiwan

[4] Institute of Plant and Microbial Biology, Academia Sinica, Taipei 115201, Taiwan

[5] Genome and Systems Biology Degree Program, National Taiwan University, Taipei 106319, Taiwan

[6] These authors contributed equally

[7] Lead contact

[†]Correspondence: syting@gate.sinica.edu.tw

Keywords:

Papain-like cysteine protease, Antibacterial toxin, DNA topoisomerase, Interbacterial antagonism

Summary

Bacteria secrete a diverse array of toxic effectors to antagonize competitors, profoundly influencing the composition of microbial communities. Previous studies have identified an interbacterial toxin predicted to exhibit proteolytic activity that is broadly distributed among Gram-negative bacteria. However, the precise mechanism of intoxication remains unresolved. Here, we demonstrate that one such protease toxin from *Escherichia coli*, Cpe1, disrupts DNA replication and segregation by recognizing and cleaving conserved sequences in the essential type II DNA topoisomerases GyrB and ParE. Cpe1 belongs to the papain-like cysteine protease family and is associated with toxin delivery pathways, including the type VI secretion system and contact-dependent growth inhibition. The crystal structure of Cpe1 in complex with its immunity protein reveals a neutralization mechanism involving competitive substrate binding rather than active site occlusion, distinguishing it from previously characterized effector-immunity pairs. Collectively, our findings unveil a unique mode of interbacterial intoxication and provide insights into how bacteria protect themselves from self-poisoning by protease toxins.

Introduction

Bacteria in natural environments exist within complex communities, where interactions—both cooperative and antagonistic—are pivotal to their survival. A key aspect of bacterial competition is the acquisition of limited resources, which has driven the evolution of a wide array of interbacterial antagonistic mechanisms, including the production of antibiotics, antimicrobial peptides, and diffusible proteinaceous toxins[1,2]. More recently, sophisticated mechanisms for distinguishing kin and antagonizing competitors have been identified[3-8]. Among these, Gram-negative bacteria utilize specialized secretion systems, such as contact-dependent growth

45 inhibition (CDI), the type IV secretion system (T4SS), and the type VI secretion system (T6SS),
46 to translocate toxins into neighboring cells in a contact-dependent manner, whereas Gram-positive
47 bacteria rely on the Esx secretion system for similar antagonistic interactions[9]. These secretion
48 systems allow pathogenic bacteria to establish dominance in polymicrobial infections and enable
49 commensal bacteria to establish compatibility within microbial consortia[10-12].

50 Interbacterial toxins delivered via these systems enhance the competitive fitness of the
51 producing bacteria by inhibiting or killing competitors. Depending on their biochemical properties,
52 the impact of these effectors on target cells can vary considerably. For instance, a wide variety of
53 antibacterial toxins induce cell lysis by disrupting the cellular membrane or degrading cell wall
54 peptidoglycans[9,13-17]. Pore-forming toxins exert their toxicity by inserting themselves into the
55 cellular membrane and causing its depolarization[18-20]. Some toxins are translocated into the
56 cytoplasm, where they compromise DNA/RNA integrity or deplete the cellular energy resources
57 of target cells[21-26]. Post-translationally modified toxins have been found to target essential proteins
58 involved in bacterial cell division and protein synthesis[27-30]. This broad spectrum of targets allows
59 the toxins to act across phylogenetically diverse bacteria. Most of the intoxication mechanisms of
60 these antibacterial toxins are inherently indiscriminate. Therefore, bacteria encode specific
61 immunity proteins adjacent to their cognate toxin genes to prevent self-intoxication or harm to kin
62 cells. These immunity proteins typically neutralize toxins by occluding their active sites[31]. In some
63 cases, other neutralization mechanisms, such as enzymatic antagonism of effector activity or
64 structural disruption of the effector domain, have also been reported[27,32].

65 Although significant progress has been made in identifying novel interbacterial toxins in
66 recent years, detailed characterizations of their intoxication mechanisms remain lacking[33-35]. For
67 example, comparative genomic, advanced genetic screening, and structure-based searching

68 approaches have uncovered novel effectors with conserved catalytic residues indicative of protease
69 and peptide amidase activities, which inhibit bacterial growth during interbacterial competition[36-
70 38]. However, their natural substrates and precise biochemical activities have yet to be elucidated.
71 In this study, we describe an interbacterial toxin that targets the essential type II DNA
72 topoisomerases GyrB and ParE via papain-like cysteine protease (PLCP) activity. This toxin is
73 phylogenetically widespread and shares hallmarks of interbacterial effectors secreted via the T6SS
74 and CDI pathways. Homologs of this toxin are similar to PLCPs associated with ATP-binding
75 cassette (ABC) transporters involved in bacterial protein export. However, their role in
76 interbacterial antagonism, specifically in targeting and damaging essential proteins, has not been
77 elucidated. Interestingly, our structural analyses further reveal that protection against the PLCP
78 toxins is conferred by cognate immunity proteins, which block substrate binding rather than
79 occlude the active site, thereby inactivating the toxicity. Our findings not only expand our
80 understanding of protease effectors in interbacterial conflict but also uncover a previously
81 undescribed mode of immunity protection.
82

83 ## Results

84 **Papain-like Cysteine Protease Antibacterial Effectors Are Found in Different Gram-negative**
85 **Bacteria**

86 Previous studies on T6SS–associated protease effectors, such as EvpQ from *Edwardsiella*
87 *piscicida* and TsaP from *Escherichia coli*, have predicted their classification within the family of
88 PLCPs[36,37]. The defining feature of this protease family is a conserved catalytic triad, consisting
89 of a cysteine (Cys) thiol group, a histidine (His) imidazolium ring, and a third residue—either
90 aspartate (Asp) or asparagine (Asn)—that orients and activates the imidazolium ring for peptide

91 bond hydrolysis (**Figure 1a**). PLCPs in bacteria have been well characterized for their roles as
92 virulence factors in both animal and plant infections[39-41], as well as for functioning as maturation
93 proteases in a variety of ABC transporters, where they specifically recognize and cleave signal
94 peptides before substrate export[42-44]. However, their function as antibacterial toxins has yet to be
95 fully understood[33].

96 To explore the prevalence of PLCPs involved in interbacterial antagonism, we conducted
97 a homology search against the National Center for Biotechnology Information (NCBI) non-
98 redundant database using PSI-BLAST[45], employing the cysteine protease domains of EvpQ and
99 TsaP as queries[36,37]. Homologous genes with more than 10% sequence identity were retrieved, and
100 their gene neighborhoods were analyzed to infer potential roles in interbacterial competition. The
101 low sequence identity threshold was selected to ensure identification of both EvpQ- and TsaP-like
102 proteins. Consequently, we identified 155 unique genes encoding PLCP domains associated with
103 either the T6SS or CDI pathways. Of these, 70 were located at the C-terminus of T6SS toxin-
104 delivery proteins (*e.g.*, PAAR, VgrG, and Rhs)[46,47], and the remaining 85 were linked to the CdiA
105 carrier protein in the CDI pathway[48] (**Figure 1b, Supplementary Figure 1a,** and **Supplementary**
106 **Table 1**). Multiple sequence alignments of these homologs, along with representative PLCPs from
107 ABC transporters (*e.g.,* ComA and LahT), confirmed the presence of the conserved catalytic triad
108 (Cys, His, Asp/Asn)[49,50] (**Figure 1c**).

109 Phylogenetic analysis of the identified protease domain sequences revealed close
110 similarities to EvpQ and TsaP[36,37] (**Figure 1d** and **Supplementary Figure 2**). These toxin
111 homologs are distributed across Phylum Pseudomonadota, including in Alpha-, Beta-, Gamma-,
112 and Delta-proteobacteria, and they are found in bacteria across a range of ecological niches,
113 including within animal and insect hosts and in the environment. Additionally, fifteen T6SS–

114 associated homologs were identified in distantly related phyla, such as Acidobacteriota,
115 Actinomycetota, Chloroflexota, Cyanobacteria, and Myxococcota (**Figure 1d, Supplementary**
116 **Figures 1-2,** and **Supplementary Table 1**). Although we detected no clear correlation between
117 phylogeny, taxonomy, and toxin-delivery pathway, the phylogenetic similarity of these homologs
118 from diverse phyla implies that horizontal gene transfer may have contributed to the evolutionary
119 dissemination of PLCP toxins.

120 To prevent self-intoxication, toxin-producing bacteria carry immunity proteins, typically
121 encoded adjacent to the toxin genes in the genome[31]. Consistent with this scenario, we found that
122 the majority of the identified PLCP toxin genes are followed in the respective genomes by putative
123 immunity genes (**Figure 1b** and **Supplementary Figure 1b**). The putative immunity proteins
124 range from 79 to 239 amino acids and exhibit considerable sequence divergence, likely reflecting
125 their specificity towards their cognate PLCP toxins. Supporting this idea, the sequence identity
126 between each immunity gene and its corresponding PLCP toxin is positively correlated, evidencing
127 their coevolutionary nature (**Supplementary Table 1**). Together, these findings suggest that PLCP
128 toxins, along with their cognate immunity proteins, are found in various Gram-negative bacterial
129 species. For clarity in this study, we have designated the identified PLCP toxin as Cpe1 (cysteine
130 protease effector 1) and the cognate immunity protein as Cpi1 (**Figures 1b, d**).

131

132 **The Structure of the Cpe1–Cpi1 Complex Reveals a Distinct Toxin-Neutralization**
133 **Mechanism**

134 Pioneering studies by Li *et al.* and Lu *et al*. have demonstrated that bacteria, such as *E.*
135 *piscicida* and *E. coli*, utilize T6SS–associated Cpe1 effectors to mediate interbacterial
136 antagonism[36,37]. However, the precise mechanisms underlying Cpe1-induced toxicity remain

137 unclear. To elucidate the mode of action of Cpe1, we employed structural biology approaches to
138 gain insights into its toxic activity. Notably, overexpression of the Cpe1 toxin domain ($Cpe1_{tox}$) in
139 *E. coli* cells resulted in growth inhibition, yielding insufficient amounts of purified protein for
140 structural analyses (**Figure 2a**). Time-lapse microscopy revealed that this growth inhibition was
141 accompanied by reduced cell proliferation and continued elongation, consistent with the proposed
142 cytotoxic activity of Cpe1[37] (**Figure 2b** and **Videos 1-2**). To circumvent this limitation, we co-
143 purified $Cpe1_{tox}$ with its cognate immunity protein, Cpi1, which allowed us to obtain well-
144 diffracting crystals (**Supplementary Figure 3a**). Using selenomethionine-substituted protein, we
145 determined the crystal structure of the $Cpe1_{tox}$–Cpi1 complex at a resolution of 1.87 Å (**Figure 2c**
146 and **Supplementary Table 2**).

147 In our crystal structure, Cpe1 features a six-stranded antiparallel β-sheet flanked by five α-
148 helices on either side, forming the typical α/β core that is characteristic of the PLCP family[51]. The
149 catalytic triad—Cys, His, Asp—is clearly evident and aligns with prior functional predictions[33,51]
150 (**Figure 2c**). Despite sharing limited sequence identity with ABC transporter-associated proteases,
151 a structural homology search using the DALI server identified ComA (Z-score = 16.3; RMSD of
152 1.9 Å across 121 aligned Cα atoms) and LahT (Z-score = 15.9; RMSD of 1.8 Å across 117 aligned
153 Cα atoms) as the closest homologs[50,52,53] (**Figure 2d**). A structural comparison revealed a high
154 conservation of the spatial arrangement of the catalytic triad of Cpe1. Overlaying the Cα atom of
155 the Cpe1 and LahT catalytic residues yielded minor RMSD values (Cys: 0.583Å; His: 0.843Å;
156 Asp: 0.711Å), whereas the catalytic triad of ComA presented a slight shift relative to Cpe1 (RMSD:
157 Cys: 2.444Å, His: 1.812Å, Asp: 1.680Å) with a 39.4° rotation of the cysteine residue (**Figure 2d**).
158 These differences may reflect variations in substrate specificity or catalytic efficiency. Overall, the

159 resolved Cpe1 structure is consistent with its predicted protease function, indicating that its
160 proteolytic activity relies on the common catalytic thiol mechanism (**Figure 1a**).

161 In line with our structural data, mutational analyses revealed that the substitution of the
162 catalytic cysteine with alanine ($Cpe1_{tox}^{C362A}$) abolished Cpe1-mediated toxicity (**Figure 2a**).
163 Moreover, the catalytically inactive Cpe1 mutant failed to induce the cell elongation phenotype
164 observed for wild-type Cpe1, further demonstrating that Cpe1 toxicity is linked to its PLCP activity
165 (**Figure 2b** and **Video 3**). To assess if the catalytic activity of Cpe1 is important for interbacterial
166 antagonism, we performed a growth competition assay using an *E. coli* strain (ATCC-11775)
167 harboring the wild-type Cpe1 toxin and an active T6SS as the donor strain, competing against a
168 recipient *E. coli* model strain (MG1655). Notably, recipient cells exhibited a significant fitness
169 defect when co-cultured with donor cells expressing wild-type Cpe1 (**Figure 2e**). However, this
170 competitive advantage was markedly reduced when donor cells expressed the inactive Cpe1
171 ($Cpe1_{tox}^{C362A}$). These findings demonstrate that the catalytic activity of Cpe1 plays a crucial role
172 in mediating interbacterial competition.

173 Interestingly, although Cpi1 binds to Cpe1 and they share a large interface (1050 $Å^2$), our
174 crystal structure reveals that Cpi1 does not sterically occlude the active site of Cpe1. Instead, Cpi1
175 primarily interacts with a shallow hydrophobic concave region on the surface of Cpe1 that is
176 located adjacent to the catalytic pocket (**Figures 2c, f**). This binding region consists of a cluster of
177 non-polar residues—L387, M390, A408, M426, W428, and V434—the hydrophobic properties of
178 which are conserved across many T6SS– and CDI–associated Cpe1 toxins (**Supplementary**
179 **Figure 1a**). We did not identify any enzymatic domain in or significant structural homologs of
180 Cpi1, suggesting that its neutralization mechanism depends on binding to the hydrophobic concave
181 region of Cpe1 rather than occlusion of its active site.

182 To examine the importance of the Cpe1–Cpi1 interaction, we assessed the ability of Cpi1
183 variants displaying impaired Cpe1 binding to protect against toxicity. By scanning the Cpe1–Cpi1
184 interface, we identified four candidate residues (I47, M61, M64, and K72) in Cpi1, where
185 substitutions were predicted to disrupt the Cpe1–Cpi1 interaction (**Figures 2g**). Single-residue
186 substitutions did not significantly affect the ability of Cpi1 to inhibit Cpe1 toxicity, as these
187 variants retained their immunity function and still bound Cpe1 in co-immunoprecipitation assays
188 (**Figures 2h, i**). However, when we mutated all four residues ($Cpi1^{mut4}$), the resulting mutant
189 lacked the ability to neutralize Cpe1 toxicity and failed to bind Cpe1 *in vitro*, despite being
190 expressed at levels comparable to that of wild-type protein (**Figures 2h, i**, and **Supplementary**
191 **Figure 3b**). In addition, the Cpi1 quadruple mutant did not provide full protection during
192 interbacterial competition (**Figure 2e**). These findings indicate that the interaction between Cpe1
193 and Cpi1 is critical for the immunity function of Cpi1 and that disruption of this interaction
194 abrogates its protective effect (**Figures 2a, b**, and **Video 4**).
195
196 **The Hydrophobic Concave Surface Is Critical for Cpe1 Toxicity**
197 Our structural analysis revealed that Cpe1 shares significant similarities with the cysteine
198 protease domains of ComA and LahT[50,52] (**Figure 2d**). Previous biochemical and structural studies
199 of these proteases have shown that, similar to Cpe1, they also possess hydrophobic concave
200 surfaces adjacent to their catalytic pockets, which are critical for specific recognition of protein
201 substrates[50,52] (**Supplementary Figure 4**). Previous studies have also shown that blocking these
202 hydrophobic regions with high-affinity inhibitors leads to protease dysfunction and impaired
203 substrate transport[50,54]. Given that Cpi1 neutralizes Cpe1 toxicity by interacting with its
204 hydrophobic concave region (**Figure 2f**), we hypothesized that Cpe1 might employ a substrate

205 recognition mechanism analogous to that of ComA and LahT. To test this hypothesis, we
206 introduced mutations into hydrophobic residues within the concave region of Cpe1 (*i.e.,* L387,
207 M426, W428) and assessed their impact on toxicity (**Figure 2f**). Supporting our hypothesis,
208 ectopic expression of the Cpe1 variants in model *E. coli* resulted in a marked reduction in toxicity
209 compared to wild-type Cpe1, without affecting protein expression levels (**Figure 3a**). These
210 findings support the notion that the hydrophobic concave region is important for the cytotoxic
211 activity of Cpe1 and may also contribute to substrate recognition.

212 To further investigate if the hydrophobic concave region of Cpe1 is involved in substrate
213 binding, we carried out site-specific photo-crosslinking experiments, focusing on the residues for
214 which mutations abolished Cpe1-mediated toxicity (**Figure 3a**). We incorporated the photo-
215 reactive amino acid p-benzoyl-L-phenylalanine (Bpa) in place of the selected amino acids using
216 enhanced nonsense suppression[55] (**Figure 3b**). This crosslinking approach provides several
217 advantages, including the ability to introduce the Bpa crosslinker at a single site within Cpe1, and
218 its modestly larger size relative to phenylalanine increases the likelihood of capturing direct
219 interactions with substrates[56]. To prevent Cpe1 from cleaving its bound substrates, we introduced
220 the catalytically inactive C362A mutation into the Cpe1-Bpa variants for our crosslinking
221 experiments.

222 Cells expressing these Cpe1-Bpa variants were directly exposed to long-wavelength UV
223 irradiation (365 nm) to induce covalent crosslinking between Cpe1 and potential substrates
224 (**Figure 3b**). Following UV exposure, Cpe1-Bpa and its crosslinked products were purified using
225 the hexa-histidine tag located at the C-terminus of Cpe1 and analyzed by electrophoresis and
226 immunoblotting. As expected, we observed multiple crosslinked products migrating more slowly
227 by SDS-PAGE than Cpe1-Bpa monomers (*i.e.,* L387Bpa, M426Bpa, W428Bpa) (**Figure 3c**). The

228 molecular weights of the crosslinked products ranged from 30 kDa to 180 kDa, indicating
229 formation of Cpe1-substrate complexes. In contrast, our control samples, which did not incorporate
230 Bpa, presented no high-molecular-weight crosslinked adducts on the gels. Additionally, levels of
231 the Cpe1-Bpa monomers (L387Bpa, M426Bpa, W428Bpa) slightly decreased after UV irradiation,
232 further supporting that Cpe1-Bpa bound and crosslinked to its substrates via the hydrophobic
233 concave region. This decrease in level upon UV irradiation was not observed for a parallel control
234 experiment, indicating that the crosslinking was specific to the modified Cpe1-Bpa variants
235 (**Figure 3c**).
236
237 **Cpe1 Targets the Essential Type II DNA Topoisomerases GyrB and ParE**
238 To define potential protein substrates of the Cpe1 toxin, we subjected purified Cpe1-Bpa
239 crosslinked adducts to mass spectrometric analysis. To minimize false-positive results that could
240 obscure our identification of physiological targets, we applied a stringent cutoff, focusing on
241 proteins with >10 unique peptides, an intensity index >5, and consistent detection across three
242 replicates. Given that many interbacterial toxins associated with the T6SS and CDI pathways are
243 known to target essential cellular components to inhibit or kill competing cells[48], we focused our
244 analysis on essential proteins, though we are aware that non-essential proteins might also
245 contribute to critical cellular processes.
246 Our mass spectrometry analysis revealed 51 cytosolic proteins that were consistently
247 detected across all three Cpe1-Bpa crosslinking experiments (**Supplementary Table 3**). Among
248 these, eight were identified as essential for *E. coli* viability, each playing a critical role in diverse
249 cellular processes[57,58]. These proteins included the type II DNA topoisomerases GyrB and ParE,
250 essential for DNA replication and chromosome segregation; NusA, NusG, and RpoB, involved in

251 transcription; FtsZ, critical for cell division; and AccA and DapE, vital for metabolism (**Figure**
252 **3d**).

253 To validate the substrates of Cpe1, we performed an *in vitro* protease cleavage assay by
254 incubating purified candidate target proteins with $Cpe1_{tox}$. In this assay, $Cpe1_{tox}$ is expected to
255 recognize and cleave the targets, with proteolytic cleavage being confirmed by SDS-PAGE
256 analysis, whereby a reduction in molecular weight and the presence of cleavage fragments
257 indicated substrate digestion. As a result, we observed that two out of the eight essential proteins—
258 type II DNA topoisomerases GyrB and ParE—displayed clear molecular weight reductions upon
259 being incubated with $Cpe1_{tox}$ but not with the catalytically inactive $Cpe1_{tox}^{C362A}$ (**Figures 3e, f** and
260 **Supplementary Figures 5a-f**). Moreover, adding the immunity protein Cpi1 to the reaction
261 inhibited the proteolytic activity of Cpe1 (**Supplementary Figures 5g, h**). Notably, incubating
262 either GyrB or ParE with wild-type $Cpe1_{tox}$ resulted in relatively short but consistent fragments
263 (~12 to 14 kDa), indicating that the cleavage events are specific and may occur toward the termini
264 of these proteins. Collectively, these findings support a model in which Cpe1 targets the essential
265 proteins GyrB and ParE, potentially impairing vital cellular functions as part of a competitive
266 inhibition strategy.

267

268 **Cpe1 Cleaves a Consensus Sequence Containing Double Glycine Motifs within GyrB and**
269 **ParE**

270 Many proteases in the PLCP family cleave peptide bonds at sequence-specific sites[51].
271 Notably, homologs of Cpe1, such as ComA and LahT, recognize and cleave their native substrates
272 at sequences containing a double glycine (GG) motif[50,59,60] (**Supplementary Figures 6a, b**).
273 Accordingly, we hypothesized that Cpe1 might also target its substrates, GyrB and ParE, at a

274 consensus sequence containing two consecutive glycine residues. Protein sequence alignment of
275 GyrB and ParE revealed four consensus sequences containing GG motifs (**Figure 3g**). Two of
276 these motifs, located near the N-terminal ATPase domain: $G_{101}G_{102}$ and $G_{113}G_{114}$ in GyrB, and
277 $G_{97}G_{98}$ and $G_{109}G_{110}$ in ParE, were prioritized for further investigation, as cleavage at these sites
278 would generate ~12 to 14 kDa fragments, *i.e.,* matching those observed in our *in vitro* cleavage
279 assays (**Figures 3e, f**).

280 To confirm these cleavage sites, we purified variants of GyrB and ParE in which one
281 glycine residue had been deleted from each GG motif, and then subjected them to $Cpe1_{tox}$ cleavage
282 assays. Our results showed that removing one of the $G_{101}G_{102}$ residues in GyrB or from $G_{97}G_{98}$ in
283 ParE significantly reduced $Cpe1_{tox}$-mediated cleavage (**Figures 3h, i**). In contrast, mutations in the
284 other GG motifs had no effect on cleavage by $Cpe1_{tox}$. Consistent with this outcome, we were able
285 to identify the tryptic peptides, mapping to Cpe1-cleaved GyrB and ParE via in-gel digestion
286 followed by mass spectrometry analysis (**Supplementary Figures 6c, d**). Together, these findings
287 support the notion that Cpe1 selectively targets consensus sequences containing the $G_{101}G_{102}$ motif
288 in GyrB and the $G_{97}G_{98}$ motif in ParE, reinforcing the substrate specificity of Cpe1 (**Figure 3g**).

289

290 **Cpe1-mediated Proteolysis Disrupts DNA Topology and Inhibits Chromosome Segregation**
291 **in Bacteria**

292 GyrB and ParE are members of the type II DNA topoisomerases, forming the hetero-
293 tetrameric DNA gyrase ($GyrB^2/GyrA^2$) and topoisomerase IV ($ParE^2/ParC^2$) complexes,
294 respectively, in bacteria[61]. These enzymes are well characterized for their roles in catalyzing the
295 relaxation of supercoiled DNA in an ATP-dependent manner, thereby facilitating critical biological
296 processes that require modification of DNA topology[62]. Malfunction of DNA gyrase impairs DNA

297 replication, transcription, and repair, whereas inhibition of topoisomerase IV results in abnormal
298 catenation of daughter chromosomes following replication, ultimately blocking cell division[63].
299 These essential activities make both proteins appealing targets for antimicrobial agents in clinical
300 settings[64,65]. Notably, the consensus sequence recognized by Cpe1 is located within a loop
301 connecting helix 3 and helix 4 in the ATPase domain of GyrB and ParE[66,67] (**Figures 4a, b**). This
302 loop is highly conserved across different bacterial species[68] (**Figures 4c, d**), and has been
303 previously identified as a critical region involved in ATP-binding, dimerization, and
304 conformational changes triggered by ATP hydrolysis[67,69,70]. Therefore, cleavage of the loops in
305 GyrB and ParE by Cpe1 would paralyze topoisomerase function, conferring a competitive fitness
306 advantage to antagonistic bacteria by inhibiting DNA replication and chromosome segregation in
307 their rivals.

308 If GyrB and ParE are indeed substrates of Cpe1, we reasoned that Cpe1 intoxication would
309 impair the ability of both enzymes to maintain DNA topology, specifically by decreasing negative
310 supercoiling of cellular DNA. Therefore, we used a high-copy plasmid, pET, isolated from *E. coli*
311 ectopically expressing Cpe1 to visualize changes in DNA topology via high-resolution agarose gel
312 electrophoresis with chloroquine, allowing the resolution of negatively supercoiled DNA. As
313 predicted, plasmid DNA topoisomers extracted from Cpe1-intoxicated cells (0.5 and 1 hour of
314 induction) displayed a significant decrease in negatively supercoiled DNA bands[71] (**Figure 4e**). In
315 contrast, plasmid DNA from cells expressing the catalytic mutant Cpe1^{C362A} showed a high level
316 of plasmid DNA in a relaxed state, *i.e.,* similar to the vector control. This observation mirrors the
317 effects reported previously when the ATPase domains of GyrB or ParE were inhibited or mutated,
318 supporting that the observed changes were attributable to disruption of type II DNA topoisomerase
319 activity[69,72,73].

320 Inactivation of topoisomerase IV is known to result in DNA knotting and catenation,
321 leading to an accumulation of unsegregated DNA at the center of bacterial cells[74]. Fluorescence
322 microscopy validated this notion, revealing unsegregated and condensed DNA in elongated
323 bacteria subjected to Cpe1 intoxication (**Figure 4f** and **Supplementary Figure 7**), representing a
324 phenotype reminiscent of cells treated with novobiocin, an antibiotic that inhibits the ATPase
325 activities of both GyrB and ParE[75,76]. In contrast, sister nucleoids formed and segregated normally
326 in dividing cells expressing either the Cpe1^{C362A} variant or those co-expressing Cpe1 and its
327 cognate immunity protein, Cpi1 (**Figure 4f** and **Supplementary Figure 7**). Given that
328 chromosome partitioning is critical for successful cell division, next we examined if Cpe1
329 intoxication also disrupts the bacterial cell division machinery. To test this possibility, we
330 conducted Cpe1 intoxication experiments on *E. coli* expressing fluorescently labeled cell division
331 protein FtsZ (*i.e.,* FtsZ-mNeonGreen)[77]. As expected, the Z-ring structure that is essential for cell
332 division failed to form at the septa of Cpe1-intoxicated bacteria (**Supplemental Figures 8a, b**).
333 These findings collectively support a model in which Cpe1 targets and cleaves the consensus loops
334 in ATPase domains of GyrB and ParE, disrupting their topoisomerase activity and thereby
335 inhibiting DNA replication, chromosome segregation, and cell division, ultimately resulting in the
336 cessation of bacterial growth (**Figure 4g**).
337

338 **Cpi1 Confers Competitive Inhibition against Cpe1**

339 Our identification of GyrB and ParE as substrates of Cpe1 prompted us to investigate the
340 mechanism by which Cpi1 inhibits Cpe1. Based on the Cpe1$_{tox}$–Cpi1 complex structure, toxicity
341 assays, and site-specific crosslinking experiments, we suspected that Cpi1 binds competitively at
342 the hydrophobic concave region of Cpe1, overlapping with the binding regions of GyrB and ParE,

343 thereby neutralizing Cpe1-mediated intoxication. This competitive inhibition model was supported
344 by AlphaFold3 (AF3) predictions, which revealed that the binding regions for GyrB and ParE on
345 Cpe1 partially overlap with those of Cpi1 in the predicted structures[78] (**Figure 5a**, and
346 **Supplementary Figures 9a, b**). Notably, the loop sequence containing the Cpe1 cleavage site on
347 GyrB actually extends into the catalytic pocket of Cpe1 in the AF3 model structure, supporting our
348 prior characterization of its protease activity and substrate specificity (**Supplementary Figure 9c**).
349 To test the competitive inhibition model, we began by conducting *in vitro* competitive
350 binding assays to determine if Cpi1 could displace substrate interactions with Cpe1 (**Figure 5b**).
351 In our assay, catalytically inactive $Cpe1^{C362A}$ was incubated with the substrate (*e.g.,* the ATPase
352 domain of ParE), which was tagged with a C-terminal strep tag to allow complex formation. The
353 Cpe1/ParE complex was then immobilized on streptavidin resin. The ATPase domain of ParE
354 served as a representative substrate due to its ease of purification and susceptibility to cleavage by
355 wild-type Cpe1, similar to full-length ParE (**Supplementary Figure 9d**). Following complex
356 formation, increasing concentrations of wild-type Cpi1 were added, followed by washing to
357 remove unbound $Cpe1^{C362A}$. As a result, $Cpe1^{C362A}$ levels bound to $ParE_{ATPase}$ were markedly
358 reduced in the presence of Cpi1 in a concentration-dependent manner, indicating that Cpi1
359 displaced $ParE_{ATPase}$ from its interaction with $Cpe1^{C362A}$ (**Figure 5c**). In contrast, in a control
360 experiment using $Cpi1^{mut4}$, in which the Cpe1-binding residues had been mutated (**Figure 2j**), no
361 significant changes in $Cpe1^{C362A}$ level were observed (**Figure 5d**). These findings support that
362 Cpi1 competitively interacts with the substrate-binding site on Cpe1. Based on the observed
363 competition, we reasoned that Cpi1 should exhibit a higher binding affinity to Cpe1 than its target
364 substrates. Using biolayer interferometry, we confirmed that Cpi1 binds to $Cpe1^{C362A}$ with an
365 approximately 40-fold higher affinity than $ParE_{ATPase}$ *in vitro* (K_d: $Cpe1^{C362A}$ –Cpi1 = 8.58 nM;

366 Cpe1^{C362A}–ParE$_{ATPase}$ = 343 nM). However, binding affinity was too low to be measured when
367 Cpi1^{mut4} was used (**Figures 5e, f** and **Supplementary Figure 9e**). Collectively, these results
368 support a model whereby Cpi1 neutralizes Cpe1-mediated intoxication by employing a
369 competitive inhibition mechanism.
370

371 ## Discussion

372 Our study characterizes a widely distributed class of antibacterial effectors displaying
373 papain-like cysteine protease activity, referred to herein as Cpe1, which is found in diverse Gram-
374 negative bacteria. By targeting essential cellular processes in bacteria, these Cpe1 effectors play a
375 critical role in bacterial competition, broadening the known repertoire of bacterial toxins involved
376 in interbacterial antagonism. We have demonstrated that Cpe1 exerts its toxic effect by cleaving
377 key protein substrates, specifically the type II DNA topoisomerases GyrB and ParE, which are
378 indispensable for DNA replication and chromosome segregation. Cpe1 mediates this cleavage by
379 targeting consensus sequences containing GG motifs within the ATPase domains of these proteins,
380 thereby inactivating the topoisomerase function and halting the DNA replication machinery and
381 cell growth. This mechanism provides a competitive advantage to Cpe1-producing strains.

382 Our phylogenetic analysis reveals a complex evolutionary trajectory for Cpe1 homologs,
383 underscoring their occurrence across diverse bacterial phyla and their functional association with
384 secretion systems such as the T6SS and CDI pathways (**Figure 1d**). The broad distribution of Cpe1
385 homologs indicates that horizontal gene transfer has facilitated adaptation of these protease
386 effectors to diverse ecological niches, enabling bacteria to assert competitive dominance in various
387 environments. Furthermore, the lack of correlation between phylogeny and pathway association
388 among Cpe1 homologs supports that selective pressures favor the adoption of Cpe1-like effectors

389 across multiple bacterial lineages, thereby enhancing bacterial fitness in different ecological
390 contexts.

391 Papain-like cysteine proteases are versatile enzymes that cleave peptide bonds in protein
392 targets and are frequently employed as toxic effectors by bacterial pathogens. For example, the
393 bacterial effector OspD3, secreted by *Shigella flexneri*, cleaves host kinases RIPK1 and RIPK3 to
394 evade necroptosis-mediated immune responses during infection[39]. Similarly, the YopT effector
395 from *Yersinia sp.* cleaves Rho-family GTPases, such as RhoA, leading to disruption of the actin
396 cytoskeleton[79]. Additionally, AvrPphB from *Pseudomonas syringae*, induces plant cell death by
397 cleaving the PBS1 kinase through its cysteine protease activity[80,81]. Our findings provide
398 compelling evidence of bacteria leveraging a PLCP-mediated mechanism to intoxicate competing
399 bacteria, as demonstrated by Cpe1 cleavage of essential DNA topoisomerases. Given that
400 interbacterial interactions predate the evolution of eukaryotic cells, it is plausible that PLCP toxins
401 targeting eukaryotic hosts evolved from ancestral PLCPs possessing antibacterial activity.

402 We identified several cellular proteins crosslinked to Cpe1-Bpa from our crosslinking mass
403 spectrometry experiments (**Figures 3b-d**). In addition to GyrB and ParE, six other essential
404 proteins were detected, namely NusA, NusG, RpoB, FtsZ, AccA, and DapE. However, Cpe1
405 exhibited cleavage activity toward GyrB and ParE in our *in vitro* protease cleavage assays, but
406 not against these other six targets (**Figures 3e, f** and **Supplementary Figures 5a-f)**. These false-
407 positive identifications might be due to non-specific interactions with heterologous Cpe1-Bpa
408 expression. Our further analysis of the cleavage sites revealed that Cpe1 recognizes a consensus
409 sequence, LHAGGKF, within a loop region of its substrates and cleaves the peptide bond
410 immediately following the double glycine residues. Deletion of these glycine residues in GyrB and
411 ParE significantly reduced Cpe1 activity *in vitro* (**Figures 3h, i**). The contribution of other amino

412 acid residues within the consensus sequence to Cpe1 activity remains unclear, as does the influence
413 of substrate three-dimensional structure on Cpe1 specificity and cleavage. Systematic analysis of
414 cleavage sequences and structural determinants is required to determine if Cpe1 can recognize and
415 cleave additional substrates in bacteria.

416 In addition to elucidating the role of Cpe1 during interbacterial antagonism, our study
417 identifies a unique immunity mechanism that safeguards Cpe1-producing bacteria from self-
418 toxicity. The cognate immunity protein, Cpi1, binds to a conserved hydrophobic concave surface
419 adjacent to the catalytic pocket of Cpe1 (**Figure 2f**). This interaction prevents Cpe1 from accessing
420 its substrates without occluding the active site of the effector. The coevolutionary relationship
421 between Cpe1 and Cpi1 is evidenced by sequence conservation and structural complementarity.
422 The evolutionary advantage of this mode of inhibition likely lies in the enhanced binding affinity
423 afforded by the large surface area of hydrophobic interaction. Similar mechanisms have been
424 reported for other protease-inhibitor systems. For example, the anticoagulation factor triabin
425 inhibits thrombin protease by binding to regions outside of the catalytic pocket[82,83], and calpastatin
426 neutralizes calpain protease through an exosite interaction, tripling the binding surface compared
427 to other inhibitors[84,85]. Likewise, the anti-toxins of colicin, such as E3 rRNase and E9 DNase, are
428 known to neutralize these toxins by binding with high affinity to the exosites, effectively blocking
429 activity without overlapping the active site[86].

430 Bacterial toxins possessing protease activity have long been proven valuable tools in
431 investigating host cell biology due to their ability to manipulate with precision specific cellular
432 functions. For example, the identification of the protein targeted by the specific endopeptidase
433 activity of the tetanus and botulinum toxins provided fundamental insights into the role of SNARE
434 complex proteins in regulating exocytosis[87,88]. Our finding that Cpe1 specifically cleaves GyrB

435 and ParE has unveiled the possibility of applying this toxin to study DNA replication, catenation,
436 and chromosome segregation, among other aspects of cell biology. Although the general functions
437 of these topoisomerases are already well established, certain mechanistic aspects remain unclear[89].
438 Given its precise targeting of the ATPase domains of GyrB and ParE, Cpe1 could serve as a
439 valuable tool for dissecting the finer details of certain critical processes.

440 In conclusion, our study provides a detailed characterization of Cpe1 as a potent
441 interbacterial toxin that targets essential DNA topoisomerases in competitor cells. By broadening
442 the functional scope of PLCPs in bacterial competition and elucidating the molecular mechanisms
443 underlying immunity against Cpe1, our findings lay the groundwork for further exploration of how
444 PLCPs function within microbial communities. The substrate specificity and potent activity of
445 Cpe1 highlight its potential for applications in developing analogs or inhibitors that replicate its
446 targeting mechanism. Furthermore, insights into the Cpi1 immunity mechanism could inform the
447 engineering of bacterial strains presenting enhanced resistance to PLCP-mediated antagonism,
448 opening up avenues for biotechnological applications such as microbiome manipulation and the
449 creation of next-generation antibacterial therapies.

450

451 # Methods

452 **Bioinformatic Analysis of Cpe1 and Cpi1-related Proteins**

453 The protein sequences of the full-length PLCP effectors EvpQ (GenBank:
454 JACQ01000015.1, 119,565-120,092 basepairs) and TsaP (accession number: AJM72455.1) were
455 obtained from the NCBI database, as described in previous studies[36,37]. The cysteine protease
456 domains within these sequences were identified using the NCBI Conserved Domain Search tool[90]
457 and subsequently used as seed sequences for PSI-BLAST[45]. PSI-BLAST was run iteratively until

458 convergence, with a relatively lenient e-value cut-off of 0.01 to ensure inclusion of highly
459 divergent homologs. To minimize false-positive hits, the retrieved sequences were filtered to retain
460 only those with a minimum length of 100 amino acids.

461 Interbacterial PLCP effectors were manually curated based on their genomic context within
462 gene clusters associated with contact-dependent antagonistic pathways (*i.e.,* T6SS, CDI)[91,92].
463 Effector-associated domains known to mediate interbacterial antagonism, such as PAAR, VgrG,
464 and Rhs for T6SS, or VENN and filamentous hemagglutinin peptide repeats for CDI, were used
465 to validate their functional relevance[46,47]. Taxonomic and strain-level information for the identified
466 PLCP effectors was retrieved from NCBI. Multiple sequence alignments of the homologs were
467 performed using ClustalW[93], and a maximum likelihood phylogenetic tree was constructed using
468 the IQtree online tool with default parameters[94]. The resulting tree was visualized and edited using
469 Figtree (http://tree.bio.ed.ac.uk/software/figtree/).

470

471 **Bacteria and Culture Conditions**

472 The bacterial strains used in this study are listed in **Supplementary Table 4**. The following
473 *Escherichia coli* strains were used: DH5α and PIR1 for cloning and plasmid maintenance; S17-1
474 λ pir for conjugal transfer of the pRE118 plasmid into *E. coli*; and BL21 (DE3) for overproduction
475 and purification of protein samples. *E. coli* ATCC-11775 and MG1655 were used for toxicity assay
476 and bacterial competition assays. Bacterial strains were routinely grown in Luria Bertani (LB)
477 medium supplemented with appropriate antibiotics at 37°C with shaking at 200 rpm. Antibiotics
478 and chemicals were used at the following concentrations: 50 µg/mL for kanamycin, 25 µg/mL for
479 chloramphenicol, 150 µg/mL for carbenicillin, 0.25 mM isopropyl β-D-1-thiogalactopyranoside
480 (IPTG), 0.2% (*w/v*) L-(+)-arabinose, and 10% (*w/v*) sucrose.

481 **Plasmid Construction**

482 All plasmids and primers used in this study are listed in **Supplementary Table 4**.
483 Mutations in *E. coli* were generated using the pRE118 vector[95]. For chromosomal mutation
484 constructs, 800-basepair regions flanking the mutation site were amplified by polymerase chain
485 reaction (PCR), sewn together, and inserted into the vector using Gibson assembly at the *XbaI* and
486 *SacI* restriction sites[96]. Insertions at the Tn7 sites of *E. coli* strains were generated using the
487 pUC18mini R6K vector with the target genes amplified by PCR and inserted into the vector
488 through Gibson assembly at the *XhoI* and *SacI* restriction sites[97].

489 For co-expression and purification of the $Cpe1_{tox}$–Cpi1 complex, the $cpe1_{tox}$ and *cpi1* genes
490 were amplified and cloned into MCS (multiple cloning site)-1 (*BamH1* and *NotI* sites) and MCS-
491 2 (*NdeI* and *XhoI* sites) of the pETDuet-1 vector, respectively, resulting in N-terminal hexa-
492 histidine fusion to $cpe1_{tox}$. Candidate protein substrates of $Cpe1_{tox}$ were purified by cloning the
493 corresponding genes into MCS-1 of pETDuet-1. The *BamHI* and *NotI* sites were used to N-
494 terminally fuse hexa-histidine to substrates (*e.g.,* GyrB and ParE)[98]. Alternatively, the *NcoI* and
495 *NotI* sites were employed for C-terminal hexa-histidine fusions to substrates (*e.g.,* NusA, NusG,
496 RpoB, AccA, and DapE) or for expressing proteins without fusion tags (*e.g.,* FtsZ). For strep-
497 tagged proteins (*e.g.,* Cpi1 variants and the ATPase domain of ParE) and His-tagged Cpi1, the
498 corresponding genes were cloned into MCS-2 of pETDuet-1 using the *NdeI* and *XhoI* restriction
499 sites.

500 Site-directed mutagenesis was performed to generate substitution mutants of toxin and
501 immunity proteins in pBAD33 and pETDuet-1 plasmids. Primers containing the desired mutations
502 were paired with a complementary primer in the opposite orientation to amplify a mutated copy of
503 the plasmid. The template plasmid was digested using *DpnI*, and the resulting mutated amplicon

504 was transformed into *E. coli* competent cells. Mutant plasmids were selected by growth on plates
505 containing carbenicillin (for pETDuet-1) or chloramphenicol (for pBAD33).
506
507 **Generation of Mutant Strains of *E. coli***
508 To generate mutations of *E. coli* ATCC-11775 strains, mutant constructs in pRE118
509 plasmid were transformed into *E. coli* S17-1 λ pir. *E. coli* S17-1 λ pir donor strains carrying the
510 mutant constructs and *E. coli* ATCC-11775 recipient strains to be mutated were grown overnight
511 on LB plates containing appropriate antibiotics, then scraped together to create a 1:1 mixture of
512 each donor-recipient pair that was spread on an LB agar plate and incubated at 37°C for 6 hours
513 to facilitate plasmid transfer via conjugation. Cell mixtures were then scraped into LB and plated
514 on LB agar containing kanamycin and chloramphenicol to select for *E. coli* ATCC-11775 with
515 integrated plasmid. *E. coli* ATCC-11775 merodiploid strains were then grown overnight in a non-
516 selective LB medium at 37°C, followed by counter-selection by plating on nutrient agar plates
517 supplemented with sucrose. Kanamycin-sensitive, sucrose-resistant colonies were screened for
518 allelic replacement by colony PCR, and mutations were confirmed by Sanger sequencing of the
519 PCR products.
520 To generate *E. coli* MG1655 strains with insertions at the Tn7 site, pUC18mini_R6K
521 plasmids carrying the insert fragments and the helper plasmid pTNS3 were co-transformed into *E.*
522 *coli* MG1655 through electroporation[97]. Following electroporation, the cell suspension was
523 incubated in SOB media at 37°C for 1 hour for recovery. The cells were then plated onto LB agar
524 containing kanamycin for selection. Kanamycin-resistant colonies were screened for the presence
525 of insertions using colony PCR, and mutations were confirmed by Sanger sequencing of the PCR
526 products.

527 **Cpe1 Toxicity Assays**

528 To assess the toxicity of $Cpe1_{tox}$ variants and the protective effect conferred by expression
529 of Cpi1 variants, overnight cultures of *E. coli* BL21 (DE3) harboring toxin and immunity genes in
530 pBAD33 and pETDuet-1 vectors, respectively, were used to inoculate LB medium. Cultures were
531 adjusted to an initial optical density (OD_{600}) of 0.05 and incubated at 37°C with shaking at 200
532 rpm for 4 hours in the presence of appropriate inducers. Following incubation, 10-fold serial
533 dilutions of each culture were prepared and plated onto LB agar to determine colony-forming units
534 (CFUs). Unless otherwise specified, $Cpe1_{tox}$ expression was induced by the addition of arabinose
535 to cultures harboring pBAD33, whereas expression of Cpi1 from pETDuet-1 was induced by the
536 addition of IPTG.

537

538 **Bacterial Competition Assays**

539 For each competition experiment, *E. coli* ATCC-11775 Δ*hns* was used as the donor strain,
540 whereas *E. coli* MG1655 served as the recipient strain. The Δ*hns* mutation was introduced into the
541 donor strain to upregulate T6SS activity as previously described[99-101]. The indicated *E. coli* donor
542 and recipient strains were cultured for 16 hours in LB broth at 37°C. The overnight cultures were
543 then refreshed by inoculating LB medium at a ratio of 3:100 (culture:medium) and incubated at
544 37°C for 5 hours. After incubation, cells were harvested by centrifugation at 17,900 × *g* for 1
545 minute. The supernatant was discarded, and the cell pellets were washed once with LB medium.
546 The cells were centrifuged again, resuspended in LB, and normalized to an OD_{600} of 2. Donor and
547 recipient strains were then mixed at a 50:1 (*v/v*) ratio, and the initial donor-to-recipient ratios were
548 determined by performing 10-fold serial dilutions and plating on selective media. Competitions
549 were initiated by spotting 3 × 5 μL of each mixture onto nitrocellulose filters placed on LB agar

550 plates containing 3% (*w/v*) agar. The plates were incubated at 37°C for 6 hours. Following
551 incubation, cells were harvested by scraping individual spots from excised sections of the
552 nitrocellulose filter into LB medium. The suspensions were serially diluted and plated on selective
553 media to quantify CFUs.
554
555 **Analysis of Protein Expression Levels**
556 To analyze the expression of $Cpe1_{tox}$ and Cpi1 variants, *E. coli* strains harboring the
557 plasmids expressing the target proteins were cultured in LB medium supplemented with
558 appropriate inducer at 37°C. Cells were harvested at an OD_{600} of 1, and cell pellets were
559 resuspended in SDS sample buffer for analysis. The samples were boiled at 100°C for 10 minutes,
560 and then subjected to SDS-PAGE. Proteins were transferred onto nitrocellulose membranes, which
561 were then blocked in TBST buffer (10 mM Tris-HCl pH 7.5, 150 mM NaCl, 0.1% (*v/v*) Tween-20)
562 containing 5% (*w/v*) non-fat milk for 30 minutes at room temperature. Blocked membranes were
563 incubated with primary antibodies (α-His, α-Strep, or α-RNA Polymerase β) diluted in TBST for
564 1 hour at room temperature. Following incubation, the membranes were washed with TBST and
565 subsequently incubated for 30 minutes at room temperature with a secondary antibody (α-mouse
566 IgG HRP-conjugated) diluted 1:5000 in TBST. After the wash with TBST, protein detection and
567 visualization were performed using a UVP BioSpectrum 815 system.
568
569 **Protein Purification**
570 To prevent cytotoxicity during overexpression in *E. coli*, all $Cpe1_{tox}$ constructs were co-
571 expressed with Cpi1 from pETDuet-1 in *E. coli* BL21 (DE3). Stationary-phase cultures of the
572 expression strains were used to inoculate 1 liter of LB broth supplemented with carbenicillin,

573 which was then incubated in a shaking (200 rpm) incubator at 37°C until the mid-log phase (OD_{600}
574 = 0.4 - 0.7). Protein expression was induced by adding IPTG, followed by incubation at 30°C for
575 5 hours. Cells were harvested by centrifugation at 7,000 × *g* for 30 minutes and resuspended in
576 lysis buffer (50 mM Tris-HCl pH 7.5, 500 mM NaCl, 5 mM imidazole, 1 mM DTT, 5% (*w/v*)
577 glycerol, and 1 mg/mL lysozyme). Resuspended cells were incubated on ice for 30 minutes,
578 disrupted by sonication (10 pulses of 10 seconds each), and centrifuged at 40,000 × *g* for 30
579 minutes to remove cellular debris. His-tagged $Cpe1_{tox}$ and associated proteins were purified from
580 the supernatant using a 2 mL Ni-NTA agarose column by gravity flow. Bound proteins were eluted
581 using a linear imidazole gradient, reaching a final concentration of 300 mM. Purity was assessed
582 by SDS-PAGE, followed by Coomassie Brilliant Blue staining. For further purification, protein
583 samples were subjected to fast protein liquid chromatography (FPLC) using gel filtration on a
584 HiLoad 16/600 Superdex 200 pg column (GE Healthcare). Fractions demonstrating high purity
585 were collected and used in biochemical assays. For selenomethionine-incorporated $Cpe1_{tox}$–Cpi1
586 complex, cells were grown in SelenoMethionine Medium Complete (Molecular Dimensions)
587 under the same expression conditions described above. Cell lysis, Ni-NTA affinity purification,
588 and gel filtration were performed as detailed for native proteins.

589 To obtain free $Cpe1_{tox}$ for experiments, a denaturation and refolding strategy was employed
590 to separate His-tagged $Cpe1_{tox}$ from Cpi1. The protein mixture was first diluted 1:25 into
591 denaturation buffer (20 mM Tris-HCl pH 7.5, 300 mM NaCl, 1 mM DTT, and 8 M urea) to
592 denature the protein complex. Denatured proteins were then loaded onto a column containing 1
593 mL of Ni-NTA agarose, allowing selective binding of His-tagged $Cpe1_{tox}$ while dissociated Cpi1
594 was removed in the flow-through. On-column refolding was achieved by sequential washing with
595 renaturation buffer (20 mM Tris-HCl pH 7.5, 300 mM NaCl, and 1 mM DTT). The refolded protein

596 was subsequently eluted with elution buffer (20 mM Tris-HCl pH 7.5, 300 mM NaCl, and 300 mM
597 imidazole). Eluted protein samples were dialyzed against storage buffer (20 mM Tris-HCl pH 7.5,
598 300 mM NaCl, 1 mM DTT, and 5% (*w/v*) glycerol) to remove residual imidazole and stabilize the
599 protein. Dialyzed samples were then aliquoted and stored at −80°C for subsequent experiments.

600 To purify Cpe1 candidate protein substrates (GyrB, ParE, NusA, NusG, RpoB, AccA, and
601 DapE) and Cpi1, His-tagged proteins were expressed in *E. coli* BL21 (DE3) transformed with the
602 pETDuet-1 expression vector containing the corresponding coding regions. Cultures were grown
603 in LB broth at 37°C to mid-log phase and induced with IPTG, followed by 2-hour incubation at
604 37°C. Cells were harvested by centrifugation, resuspended in lysis buffer (20 mM Tris-HCl pH 7,
605 300 mM NaCl, 10 mM imidazole, 1 mM DTT, and 1 mg/mL lysozyme), and incubated on ice for
606 30 minutes. The cells were disrupted by sonication (10 pulses, 10 seconds each), and the lysate
607 was cleared by centrifugation at 40,000 × *g* for 30 minutes. His-tagged proteins were purified from
608 the supernatant by means of gravity flow through a 1 mL Ni-NTA agarose column. Proteins bound
609 to the column were eluted with a linear imidazole gradient up to 300 mM. The purity of each
610 protein sample was verified by SDS-PAGE followed by Coomassie Brilliant Blue staining.
611 Purified proteins were resuspended and dialyzed into storage buffer (20 mM Tris-HCl pH 7, 300
612 mM NaCl, 1 mM DTT, and 5% (*w/v*) glycerol). Protein aliquots were frozen and stored at −80°C
613 for further use.

614 For purification of FtsZ, FtsZ was overproduced in *E. coli* BL21 (DE3) transformed with
615 the pETDuet-1 expression vector containing the FtsZ coding region. Cultures were grown in LB
616 medium at 37°C to mid-log phase and induced with IPTG, followed by 3-hour induction at 37°C.
617 The cells were harvested by centrifugation, resuspended in lysis buffer (50 mM Tris-HCl pH 8,
618 100 mM NaCl, 1 mM EDTA, 5 mM $MgCl_2$, 1 mM PMSF, and 0.1 mg/mL lysozyme), and

619 incubated on ice for 30 minutes. Cell lysis was performed by sonication (10 pulses, 10 seconds
620 each), and the lysate was cleared by centrifugation at 40,000 × *g* for 30 minutes. To remove
621 unwanted proteins, the supernatant was subjected to ammonium sulfate fractionation. Proteins
622 precipitated at 20% (*w/v*) ammonium sulfate were discarded, whereas those precipitated at 30%
623 (*w/v*) ammonium sulfate were collected by centrifugation at 40,000 × *g* for 30 minutes. The
624 resulting pellet, enriched for FtsZ, was resuspended in buffer containing 20 mM Tris-HCl pH 8,
625 100 mM NaCl, 1 mM EDTA, and 5 mM $MgCl_2$. The resuspended proteins were dialyzed against
626 storage buffer (20 mM Tris-HCl pH 8, 100 mM NaCl, 0.1 mM EDTA, and 5% (*w/v*) glycerol),
627 aliquoted, and stored in a freezer at −80°C.

628 For purification of proteins with strep tags (*i.e.,* Cpi1 variants and the ATPase domain of
629 ParE), the proteins were overproduced in *E. coli* BL21 (DE3) transformed with the pETDuet-1
630 expression vector containing the respective gene coding regions. Cultures were grown in LB
631 medium at 37°C to mid-log phase and induced by the addition of IPTG. After 2-hour induction at
632 37°C, the cells were harvested by centrifugation and resuspended in lysis buffer (20 mM Tris-HCl
633 pH 7, 300 mM NaCl, 1 mM DTT, and 1 mg/mL lysozyme). The cells were incubated on ice for 30
634 minutes, followed by sonication (10 pulses, 10 seconds each) to achieve lysis. Cellular debris was
635 removed by centrifugation at 40,000 × *g* for 30 minutes. Strep-tagged proteins were purified from
636 the supernatant using a 1 mL gravity-flow column containing streptavidin resin (IBA Lifesciences
637 GmbH). Bound proteins were eluted with a buffer containing 20 mM Tris-HCl pH 7, 300 mM
638 NaCl, 1 mM DTT, and 2.5 mM desthiobiotin. Protein purity was evaluated by SDS-PAGE,
639 followed by Coomassie Brilliant Blue staining. Samples were further purified by means of FPLC
640 on a HiLoad 16/600 Superdex 200 pg column (GE Healthcare).
641

642 **Crystallization and Structure Determination**

643 The $Cpe1_{tox}$–Cpi1 complex was prepared for crystallization by dialyzing the purified
644 protein complex into a buffer containing 5 mM Tris-HCl (pH 7), 150 mM NaCl, and 0.5 mM tris(2-
645 carboxyethyl)phosphine (TCEP). The protein solution was then concentrated to 13.5 mg/mL using
646 spin filtration (10 kDa cutoff, Millipore). Crystallization trials were conducted using commercially
647 available screens from Hampton Research. Diffraction-quality crystals were obtained after two
648 weeks at 20°C using the hanging-drop vapor diffusion method with a protein-to-buffer ratio of 1:2.
649 The crystallization solution consisted of 0.4 M magnesium formate and 0.1 M sodium acetate (pH
650 4.6). Crystals of the selenomethionine-labeled $Cpe1_{tox}$–Cpi1 complex were grown under identical
651 conditions as the native complex, with the protein sample also concentrated to 13.5 mg/mL and
652 mixed at a 1:2 ratio with the same crystallization solution. Crystals were cryoprotected using a
653 solution of 20% (*v/v*) glycerol in the crystallization mother liquor prior to data collection.

654 Native and multiple-wavelength anomalous diffraction (MAD) datasets were collected at
655 beamlines TPS-05A and TLS-BL15A of the National Synchrotron Radiation Research Center
656 (Taiwan). Diffraction data were processed using the HKL2000 software suite[102]. Phase
657 determination was performed using PHENIX with data collected at the selenium peak wavelength
658 from selenomethionine-labeled crystals[103]. The initial model of the $Cpe1_{tox}$–Cpi1 complex was
659 constructed using the electron density map in Coot and subsequently refined using PHENIX[103,104].
660 The crystals belonged to the cubic space group P43212, with two protein complexes per
661 asymmetric unit. No residues were found in the disallowed regions of the Ramachandran plot.
662 Data collection and refinement statistics are provided in **Supplementary Table 2**.

663

664

665 **Bpa Photo-Crosslinking Experiment**

666 *E. coli* BL21 (DE3) cells were transformed with plasmids encoding $Cpe1_{tox}^{C362A}$
667 containing a TAG stop codon at specific sites (*i.e.,* L387, M426, and W428) to incorporate Bpa
668 via nonsense suppression during translation. The transformation also included the Bpa-tRNA
669 plasmid (pSUPT/BpF), which encodes the tRNA and tRNA synthetase necessary for Bpa
670 incorporation, as described previously[105].

671 The transformed cells were grown in LB medium supplemented with 1.5 mM of Bpa at
672 37°C until reaching the mid-log phase. Protein expression was induced by adding IPTG and
673 arabinose, and the cultures were incubated at 30°C for 3 hours. Cells corresponding to 50 OD_{600}
674 units were harvested, resuspended in 1 mL of ice-cold phosphate-buffered saline (PBS), and
675 divided into two aliquots. One aliquot was exposed to 365 nm UV light (Stratalinker 1800 UV
676 irradiator) for 30 minutes at 4°C to induce crosslinking, while the other aliquot was kept on ice as
677 a non-crosslinked control. Cell lysis was performed by sonication in lysis buffer (20 mM Tris-HCl
678 pH 7.5, 300 mM NaCl, 10 mM imidazole, 8 M urea, and 1 mM DTT). The lysates were incubated
679 with Ni-NTA resin for 2 hours at 4°C to purify His-tagged proteins. Bound proteins, including
680 crosslinked products, were analyzed using immunoblotting and mass spectrometry.

681

682 **Mass Spectrometry**

683 For our interactome analysis, Bpa-crosslinked $Cpe1_{tox}^{C362A}$-protein complexes were
684 purified and immobilized on Ni-NTA resins. After washing four times in lysis buffer, the resins
685 were resuspended in 8 M urea and Tris-HCl pH 8. For cysteine alkylation, 10 mM TCEP and 40
686 mM 2-chloroacetamide (CAA) were added into the samples and incubated at 45°C for 30 minutes
687 with shaking (1500 rpm). The samples were diluted 4-fold with 50 mM Tris-HCl pH 8 and digested

688 by 0.4 μg Lys-C (Wako, Japan) treatment for 3 hours at room temperature and 1 μg of trypsin
689 (Sigma, MO) overnight at 37°C. Supernatants containing digested peptides were acidified by 1%
690 TFA, desalted using the Oasis HLB 1 cc Vac Cartridge (Waters Corp), reconstituted in 80%
691 acetonitrile (ACN), and vacuum-dried at 45°C.

692 NanoLC−nanoESi-MS/MS analysis was performed on a Thermo UltiMate 3000
693 RSLCnano system connected to a Thermo Orbitrap Fusion mass spectrometer (Thermo Fisher
694 Scientific, Bremen, Germany) equipped with a nanospray interface (New Objective, Woburn, MA).
695 Peptide mixtures were loaded onto a 75 μm ID, 25 cm long PepMap C18 column (Thermo Fisher
696 Scientific) packed with 2 μm particles with a pore size of 100 Å and they were separated using a
697 segmented gradient from 5% to 25% solvent B (0.1% formic acid in ACN) in 82.5 minutes and to
698 35% solvent B in 7.5 minutes at a flow rate of 300 nL/minute. Solvent A was 0.1% formic acid in
699 water. The mass spectrometer was operated in the data-dependent mode. In brief, survey scans of
700 peptide precursors from 350 to 1600 m/z were performed at 120K resolution with a 2×10^5 ion
701 count target. Tandem MS was performed by isolation window at 1.6 daltons with the quadrupole,
702 HCD fragmentation with a normalized collision energy of 30, and MS 2 scan analysis at 30K
703 resolution in the orbitrap. The MS 2 ion count target was set to 5×10^4 and the max injection time
704 was 54 milliseconds. Only those precursors with charge states 2–6 were sampled for MS 2. The
705 instrument was run in top speed mode with 3-second cycles. The dynamic exclusion duration was
706 set to 11 seconds with a 10-ppm tolerance around the selected precursor and its isotopes.
707 Monoisotopic precursor selection was turned on. Raw data were processed using MaxQuant
708 software[106,107].

709 To identify digested peptides of Cpe1, the samples were prepared based on a previous study
710 with minor modifications[108]. The protein band from SDS-PAGE was manually excised and cut into

711 small pieces (0.5 mm^3). The excised gel pieces were washed with a solution containing 25 mM
712 NH_4HCO_3 and 40% methanol, followed by 100% ACN. The proteins in gel pieces were treated
713 with 10 mM DTT and then with 55 mM iodoacetamide. Proteins were digested with trypsin
714 (Promega) to a final substrate: trypsin ratio of 50:1 in buffer containing 25 mM ammonium
715 bicarbonate and 10% ACN for 12 to 16 hours at 37°C. The reaction was stopped by adding 5%
716 formic acid. An aliquot (0.5 µL) of the supernatant from the digest was deposited onto a 384/600-
717 µm MTP AnchorChip (Bruker Daltonik GmbH) target and allowed to air dry at room temperature.
718 Then, an aliquot (0.5 µL) of CHCA solution (1.4 mg/ml α-Cyano-4-hydroxycinnamic acid in buffer
719 containing 0.1% TFA, 1 mM ammonium phosphate, and 85% ACN) was added to the chip and
720 allowed to air dry. Further MALDI-TOF MS mass spectrometry analysis was performed in positive
721 ion mode with delayed extraction (reflection mode) on a Bruker Autoflex maX MALDI-TOF/TOF
722 mass spectrometer (Bremen, Germany) equipped with a 200 Hz SmartBean Laser. Data acquisition
723 and processing were done manually by using FlexControl 3.4 and Flex-Analysis 3.4 (Bruker
724 Daltonik GmbH), respectively. The processed data were further analyzed with Biotools 3.2 (Bruker)
725 packaged by assessing the online Mascot server to identify the corresponding polypeptides.
726
727 ***In Vitro* Protease Cleavage Assay**
728 Purified protein substrates were incubated with $Cpe1_{tox}$ (wild-type or catalytic mutant) at a
729 10:1 ratio. Reactions were performed at 20°C for 5 minutes in a final volume of 20 µL containing
730 20 mM Tris-HCl pH 7, 300 mM NaCl, and 1 mM DTT. The reactions were stopped by cooling on
731 ice and the addition of an equal volume of SDS sample buffer. Samples were boiled and analyzed
732 by SDS-PAGE, followed by Coomassie Brilliant Blue staining.
733

734 **Plasmid DNA Supercoiling Assay**

735 To visualize variations of DNA topology in bacteria, we followed the procedures described
736 in a previous study with minor modifications[109]. Overnight precultures of strains carrying
737 pBAD33-Cpe1$_{tox}$ (wild-type or catalytic mutant) and the reporter plasmid pET were refreshed in
738 LB broth and incubated at 37°C with shaking (250 rpm). When cultures reached the mid-log phase,
739 cells were transferred to a medium containing arabinose inducer and incubated for an extended
740 period to induce Cpe1$_{tox}$ expression and intoxication. Cells were pelleted by centrifugation, and
741 plasmid DNA was purified using the QIAprep Spin Miniprep Kit (Qiagen) and eluted by 50 mM
742 Tris-HCl pH 8.5. DNA topoisomers were resolved on a 1% (*w/v*) agarose gel containing Tris-
743 acetate-EDTA (TAE) and 5 μg/ml chloroquine. The gels were run in TAE buffer with 5 μg/mL
744 chloroquine for 10 hours (140 volts for 30 minutes, followed by 110 volts for 9.5 hours), stained
745 with 0.5 μg/mL ethidium bromide in TAE buffer, destained in distilled water overnight, and imaged
746 with a Quantum CX5 imaging system (Vilber).

747

748 **Fluorescence and Phase Contrast Microscopy**

749 Imaging was performed using a DeltaVision Core Deconvolution Microscopy system with
750 an Olympus IX71 microscope and a 60x 1.42 NA oil-immersion objective. For fluorescence and
751 phase contrast microscopy, bacterial cultures at the mid-log phase were used to inoculate LB
752 medium supplemented with arabinose and IPTG for the expression of Cpe1$_{tox}$ and Cpi1,
753 respectively. After 3 hours of incubation at 37°C with shaking (200 rpm), cells were harvested by
754 centrifugation at 18,000 × *g* for 1 minute. The culture supernatant was removed and washed with
755 ice-cold PBS. The washed cells were resuspended in PBS containing 70% ethanol for 15-minute
756 cell fixation on ice. The fixed cells were subjected to one PBS wash. Addition of DAPI to the cell

757 suspensions preceded a 5-minute incubation on ice in the dark. The cells were then washed with
758 PBS at 18,000 × *g* for 1 minute. The cell suspensions were then adjusted to OD_{600} = 0.5 using PBS
759 and spotted on a 1.5% (*w/v*) agarose pad settled on a microscope slide.

760 For time-lapse imaging of living cells, single colonies from LB agar were inoculated into
761 LB media supplemented with appropriate antibiotics. After incubation for 16 hours at 37°C with
762 shaking (200 rpm), the cultures were adjusted to OD_{600} = 0.5 before spotting on a 1.5% (*w/v*)
763 agarose pad containing arabinose, IPTG, and appropriate antibiotics settled on a microscope slide.
764 Phase contrast images for each sample were acquired at 10-minute intervals.

765

766 **$Cpe1_{tox}$–Cpi1/$ParE_{ATPase}$ Competitive Binding Assay**

767 His-tagged $Cpe1_{tox}^{C362A}$ protein was incubated with an excess of strep-tagged $ParE_{ATPase}$
768 for 1 hour at 4°C, followed by incubation with streptavidin resin (IBA Lifesciences GmbH). After
769 binding, the resin was washed with ice-cold buffer (20 mM Tris-HCl pH 7, 300 mM NaCl, and 1
770 mM DTT) to remove unbound proteins. Increasing concentrations of indicated Cpi1 proteins (His-
771 tagged) were added and incubated at 4°C for 1 hour, followed by a single wash with ice-cold buffer.
772 Bound proteins were eluted with buffer containing 20 mM Tris-HCl pH 7, 300 mM NaCl, 1 mM
773 DTT, and 2.5 mM desthiobiotin. Eluted samples were analyzed by SDS-PAGE, followed by
774 Coomassie Brilliant Blue staining.

775

776 **Biolayer Interferometry (BLI)**

777 BLI was performed using an 8-channel Gator® Plus instrument (Gator Bio) with Data
778 Acquisition V 2.15.5.1221 software (Gator Bio). Experiments were conducted at 30°C with
779 shaking at 1000 rpm. We immobilized 500 nM strep-tagged Cpi1, $Cpi1^{mut4}$, or $ParE_{ATPase}$ onto

780 strep-tactin XT-coated biosensor tips (IBA Lifesciences). Equilibrium binding dose-response
781 curves were generated by varying the concentrations of His-tagged $Cpe1_{tox}^{C362A}$ in BLI buffer
782 (0.2% (*w/v*) BSA, 0.02% (*v/v*) Tween-20 in PBS). For Cpi1 and $Cpi1^{mut4}$, the association and
783 dissociation intervals were conducted 150 and 300 seconds, whereas both intervals were set as 120
784 seconds for $ParE_{ATPase}$. BLI data analysis included reference channel subtraction and Savitzky–
785 Golay filtering. Kinetic parameters were determined using a 1:1 global fitting model with R_{max}
786 values linked across sensors. The interaction between $ParE_{ATPase}$ and His-tagged $Cpe1_{tox}^{C362A}$
787 exhibited fast-on-fast-off kinetics. Therefore, steady-state analysis of the response curves was
788 employed to calculate the Kd and nominal R_{max} values. All data represent results from at least three
789 independent experiments.
790
791 **Generation of Sequence Logos**
792 Protein sequences of 35,812 GyrB homologs and 14,212 ParE homologs were retrieved
793 from the UniProt database[110]. Regions containing the consensus sequence (LHAGGKF) were
794 extracted and aligned using ClustalW[93]. The results were visualized as a sequence logo using the
795 WebLogo3 online tool[111]. Sequences flanking the substrate cleavage sites were obtained from
796 previous studies to generate the sequence logo for the consensus sequences on the substrates of
797 ComA and LahT[50,60]. Sequence conservation was analyzed according to the same ClustalW
798 alignment and visualization procedures.
799
800
801
802

803 **Quantification and Statistical Analysis**

804 Statistical significance in bacterial co-culture and competition assays was assessed by
805 unpaired two-tailed t-tests between relevant samples. Values for statistical significance are
806 provided in the figure legends.

807

808 **Data Availability**

809 The coordinates and structure factors for the $Cpe1_{tox}$–Cpi1 complex have been deposited
810 in the Protein Data Bank, with accession code 9L5U.

811

812 Acknowledgments

813 We thank Drs. Harmit Malik, Dor Salomon, Jun-Yi Leu, Erh-Min Lai, Chih-Horng Kuo,
814 Chih-Yen King, and Ting laboratory members for helpful discussions; Drs. Joseph Mougous,
815 Ming-Yang Ho, Hsin-Hung Chou, and Sue Lin-Chao for sharing reagents; Dr. Hung-Ta Chen for
816 sharing equipment; Drs. Hsin-Nan Lin, Chen-Hsin Yu, Yae-Huei Liou, Sue-Ping Lee, Yung-Hsuan
817 Wu, Shu-Yu Lin, Chuan-Chih Hsu, Chin-Wen Chen, Shu-Chuan Jao, Jin-Hsuan Yu, Xin-Jie Huang,
818 and Yu-Wen Huang for technical assistance; and Dr. John O'Brien for manuscript editing. We
819 acknowledge funding support from Academia Sinica (AS-CDA-112-L05 to S.-Y.T., AS-IVA-112-
820 L05 to K.-C.H., AS-CDA-110-L01 to C.K., AS-CFII-111-201 to the Academia Sinica Biophysics
821 Core Facility, and AS-CFII-111-209 to the Academia Sinica Common Mass Spectrometry
822 Facilities) and the National Science and Technology Council, Taiwan (111-2311-B-001-006-MY2,
823 112-2311-B-001-020, and 113-2628-B-001-008-MY3 to S.-Y.T., 112-2320-B-001-006-MY3 to
824 K.-C.H., 111-2611- M001-008-MY3 to C.K.).

825

826 ## Competing interests

827 The authors declare no competing interests.

828

829 ## Figure Legends

830 **Figure 1. PLCP toxins are found in distinct Gram-negative species and are associated with**
831 **interbacterial toxin delivery pathways. (a)** The enzymatic reaction mechanism of papain-like
832 cysteine proteases (PLCPs). The catalytic triad of residues in PLCPs, composed of cysteine (Cys),
833 histidine (His), and aspartate (Asp), facilitates peptide bond cleavage. Histidine and aspartate form
834 a proton-withdrawing group that activates the cysteine residue, converting it into a nucleophile.
835 The activated cysteine attacks the carbonyl carbon of the peptide bond, leading to hydrolysis and
836 bond cleavage. **(b)** Scaled depiction of representative genomic loci from the indicated species
837 (*Edwardsiella tarda*, *Escherichia coli*, *Myxococcales bacterium*, *Roseofilum reptotaenium*,
838 *Citrobacter rodentium*, *Rhizobium* sp., *Burkholderia* sp.) encoding predicted PLCP domain-
839 containing proteins (sky blue) and putative cognate immunity proteins (yellow). Regions encoding
840 N-terminal domains of T6SS-related proteins (PAAR, VgrG, Rhs) are shaded in gray. CDI-related
841 proteins (CdiA, CdiB) are depicted in light brown. Black bars designate locations of bases
842 encoding the catalytic triads of PLCPs. Cysteine residues targeted for mutagenesis in this study
843 are depicted in red. **(c)** Sequence logo generated from alignments of PLCP domains associated
844 with bacterial contact-dependent antagonism pathways (the locus tag numbers for genes encoding
845 the sequences we used are provided in **Supplementary Table 1**). Sequences from previously
846 characterized PLCPs ($ComA_{pep}$ and $LahT_{pep}$) and recently identified T6SS-associated PLCP toxins
847 (EvpQ and TsaP) are shown below for reference. **(d)** Maximum likelihood phylogeny of PLCP
848 effectors visualized as a radiating phylogenetic tree. Taxonomy is indicated by colored shadows,

849 and delivery pathways are indicated by colored tips. The scale bar represents the average number
850 of substitutions per site. See also **Supplementary Figure 2**.
851
852 **Figure 2. Cpe1$_{tox}$-Cpi1 is a functional effector-immunity pair. (a)** Viable *E. coli* cells recovered
853 from plating cultures carrying plasmids expressing the indicated proteins on inducing media. *E.*
854 *coli* carrying plasmid-borne Cpi1 or an empty vector was included to validate suppression of Cpe1
855 toxicity. **(b)** Representative micrographs of *E. coli* cells expressing empty vector, Cpe1$_{tox}$,
856 Cpe1$_{tox}^{C362A}$, or co-expressing Cpe1$_{tox}$ and Cpi1. Frames were acquired 2 hours after induction of
857 protein expression. Scale bar, 2 μm. **(c)** Ribbon diagram representation of the X-ray crystal
858 structure of Cpe1$_{tox}$ (sky blue) in complex with Cpi1 (light gold). Residues of the catalytic triad of
859 Cpe1$_{tox}$ are indicated. **(d)** Structural alignments of Cpe1$_{tox}$ with previously characterized PLCPs:
860 ComA$_{pep}$ (PDB: 3K8U, light gray) and LahT$_{pep}$ (PDB: 6MPZ, dark gray). **(e)** Bacterial competition
861 experiments were conducted on a solid agar over a 6-hour period between the indicated donor and
862 recipient strains. *E. coli* ATCC-11775 Δ*hns* served as the donor strain, whereas *E. coli* MG1655
863 was used as the recipient strain. The Δ*hns* mutation in the donor strain was introduced to upregulate
864 T6SS activity, as described in previous studies[99-101]. **(f)** Depiction of Cpe1$_{tox}$ illustrating the
865 Cpe1$_{tox}$-Cpi1 interaction at the exosite formed by hydrophobic residues. **(g)** Magnified view of the
866 interface between Cpe1$_{tox}$ and Cpi1, highlighting the interacting residues on Cpi1 positioned near
867 the hydrophobic concave surface of Cpe1$_{tox}$. **(h)** Viable *E. coli* cells recovered from *E. coli* co-
868 expressing wild-type Cpe1$_{tox}$ and the indicated Cpi1 variants. **(i)** *In vitro* pull-down assay of
869 Cpe1$_{tox}$ and Cpi1. Cpe1$_{tox}$ proteins were pulled down by strep-tagged Cpi1 variants and
870 immobilized on streptavidin resin. Bound proteins were separated by SDS-PAGE followed by
871 Coomassie brilliant blue staining. Data in **(a)**, **(e)**, and **(h)** are represented as means ± SD. Asterisks

872 indicate significant differences ($p < 0.05$) in viability between populations **(a, h)** or statistically
873 significant differences ($p < 0.05$) between competitive indices of a given donor strain toward the
874 indicated recipients **(e)**. n.s. means no significance. See also **Supplementary Figure 3**,
875 **Supplementary Table 2**, and **Videos 1-4**.
876
877 **Figure 3. $Cpe1_{tox}$ targets and cleaves the type II DNA topoisomerases GyrB and ParE. (a)**
878 Viable *E. coli* cells recovered from expressing $Cpe1_{tox}$ with substitutions of indicated surface
879 residues from the hydrophobic concave region. The expression levels of wild-type and $Cpe1_{tox}$
880 variants were assessed by immunoblotting analysis, using the cytosolic protein RpoB as a loading
881 control (right panel). **(b)** Schematic workflow for identifying candidate substrates of $Cpe1_{tox}$
882 through Bpa crosslinking followed by LC-MS/MS protein identification. Bacteria carrying the
883 construct with a TAG stop codon at residues of interest were grown in medium supplemented with
884 Bpa. After incubation, cells were exposed to long-wavelength UV to activate formation of covalent
885 bonds between Bpa and the interacting residues. Cell lysates were incubated with Ni-NTA resin to
886 enrich for $Cpe1_{tox}$-Bpa crosslinks for further analysis. **(c)** SDS-PAGE gel analysis of crosslinked
887 protein complexes before and after UV_{365nm} treatment. $Cpe1_{tox}^{C362A}$-protein complexes enriched
888 by the Ni-NTA resin were boiled in SDS sample buffer and separated by SDS-PAGE, followed by
889 immunoblotting (α-His). **(d)** Essential proteins identified in the $Cpe1_{tox}^{C362A}$ interactome and their
890 biological functions. The complete interactome dataset is available in **Supplementary Table 3**. **(e,**
891 **f, h, i)** *In vitro* $Cpe1_{tox}$ cleavage assays. Purified $Cpe1_{tox}$ (wild-type or catalytic mutant) were
892 incubated with purified candidate substrates, *i.e.,* GyrB **(e)** and ParE **(f)**, or their variants with
893 single-glycine deletion at the predicted cleavage sites **(h, i)**, to assess hydrolysis by $Cpe1_{tox}$.
894 Fragmented proteins are marked with red arrowheads. Rxn means reaction. **(g)** Double glycine

895 motifs in the consensus regions of *E. coli* GyrB and ParE. Locations of consensus regions between
896 GyrB and ParE containing double glycine motifs are indicated on the cartoon representation of the
897 full-length proteins. The sequences of the consensus regions are shown below, with the positions
898 of the double glycine motifs labeled. The GG motif (red) and the surrounding residues (blue) are
899 highlighted.
900
901 **Figure 4. Cpe1$_{tox}$-mediated intoxication disrupts topoisomerase activity, thereby altering**
902 **DNA topology and impairing DNA replication and chromosome segregation. (a-b)** Ribbon
903 diagrams of *E. coli* GyrB (a, top structure) and ParE (b, top structure) before and after cleavage by
904 Cpe1$_{tox}$. Crystal structures of the 43-kDa ATPase domain of *E. coli* GyrB (PDB: 4PRV) and ParE
905 (PDB: 1S16) were used. Residues of the consensus sequence (LHAGGKF) are shown in yellow.
906 Structure related to the small fragments after Cpe1$_{tox}$ cleavage are indicated as pink ribbons.
907 Predicted structures after cleavage at the double glycine motif demonstrated disruption of the
908 ATPase domain of both GyrB (a, bottom structure) and ParE (b, bottom structure). **(c, d)** Sequence
909 logos evidencing conservation of the consensus sequence (LHAGGKF) of GyrB **(c)** and ParE **(d)**
910 homologs. Cleavage at the double glycine motif is indicated by dashed lines and a scissors
911 illustration. **(e)** Plasmid DNA (pET) was analyzed by high-resolution agarose gel electrophoresis
912 following isolation from *E. coli* that had expressed Cpe1$_{tox}$ or the catalytic mutant for 0.5 or 1 hour.
913 **(f)** *E. coli* cells that had expressed Cpe1$_{tox}$, Cpe1$_{tox}^{C362A}$, or Cpe1$_{tox}$ co-expressed with Cpi1 for
914 three hours. Cpe1$_{tox}$, or the catalytic mutant, was stained with DAPI (DNA; blue) and analyzed by
915 fluorescence microscopy. Phase-contrast (top), blue fluorescence (middle), and merged (bottom)
916 images are presented. Scale bar = 2 μm. Full-size images are available in **Supplementary Figure 7**.
917 **(g)** Working model of how Cpe1 intoxicates bacteria. During interbacterial competition, Cpe1

918 targets and cleaves the ATPase domains of GyrB and ParE in target cells. The cleavage leads to
919 accumulations of unrelaxed supercoils and precatenanes, disrupts DNA segregation, and ultimately
920 inhibits cell division and growth. In the Cpe1-producing cells or kin cells expressing the immunity
921 protein Cpi1, Cpe1 toxicity is neutralized through direct interaction between Cpe1 and Cpi1.
922
923 **Figure 5. Cpi1 employs a competitive inhibitory mechanism to neutralize Cpe1. (a)** The
924 $Cpe1_{tox}$-Cpi1 interface overlaps with the $Cpe1_{tox}$-substrate interaction site. Model predictions of
925 interaction between $Cpe1_{tox}$ and the ATPase domains of GyrB and ParE were constructed using
926 AlphaFold 3. See also **Supplementary Figures 9a, b** for confidence metrics. **(b)** Schematic
927 workflow for the *in vitro* competitive binding assay. Streptavidin resins bound to pre-formed
928 $Cpe1_{tox}^{C362A}$-substrate complexes were prepared and incubated with either wild-type or mutant
929 Cpi1. After incubation, the resins were washed, and the bound proteins were eluted for analysis.
930 Competitive binding events are indicated by disruption of the $Cpe1_{tox}^{C362A}$-substrate interaction,
931 leading to a decreased level of $Cpe1_{tox}^{C362A}$ in the eluted fraction due to its removal during the
932 wash step. **(c, d)** Coomassie-stained SDS-PAGE demonstrating competitive binding events. **(e, f)**
933 Kinetic analysis of interactions between Cpi1 and $Cpe1_{tox}^{C362A}$ **(e)** and $ParE_{ATPase}$ and $Cpe1_{tox}^{C362A}$
934 **(f)** using biolayer interferometry (BLI). Data from three replicates have been plotted on an X-Y
935 scatter graph. The Y-axis represents the wavelength shift generated by binding of the two proteins,
936 normalized to the calculated Rmax (% Rmax) for each run. The X-axis represents reaction time
937 (in seconds). A vertical dashed line marks the transition from the association step to the
938 dissociation step. The mean kinetic parameters (K_d, K_{on}, and K_{off}) and their standard deviations are
939 indicated.
940

941 **Supplementary Figure 1. Interbacterial PLCP effectors and their cognate immunity proteins**
942 **are distributed across various Gram-negative bacteria.** Related to **Figure 1b. (a)** Multiple
943 sequence alignment of 155 unique sequences of interbacterial PLCP effectors. Sequences have
944 been ordered by relative identity to $Cpe1_{tox}$ of *E. coli* ATCC-11775 and are displayed in two
945 clusters divided according to the associated secretion systems (T6SS or CDI). Conserved residues
946 are indicated as follows: the catalytic triad residues are highlighted by red (Cysteine) and orange
947 (Histidine and Aspartate/Asparagine) shadows; and hydrophobic residues composing the surface
948 concave region are highlighted by blue shadows. The Phylum of each strain containing the
949 interbacterial PLCP effectors is indicated by colored boxes (as indicated in the legend). **(b)**
950 Sequences of the putative cognate immunity proteins related to the interbacterial PLCP effectors
951 in **(a)**. Conserved binding residues are highlighted in green shadows. Blank rows indicate an
952 absence of putative immunity proteins due to incomplete genomic data for certain bacterial species
953 in the NCBI database. See also **Supplementary Table 1** for detailed information.
954
955 **Supplementary Figure 2. Interbacterial PLCP effectors exhibit no correlations in phylogeny,**
956 **associated secretion pathways, or taxonomy.** Related to **Figure 1d**. Maximum likelihood
957 phylogeny of 155 unique PLCP effector sequences visualized as a rectangle tree. Branch support
958 values (SH-aLRT and ultrafast bootstrap) are displayed as symbols (filled diamond: SH-aLRT ≥
959 80%, hollow diamonds: ultrafast bootstrap ≥ 95%). Tips representing sequences of the closely-
960 related housekeeping PLCPs, $ComA_{pep}$ and $LahT_{pep}$, as well as the previously identified
961 interbacterial PLCP effectors EvpQ and TsaP, are highlighted in red. The taxonomy of strains
962 containing the PLCP effectors and their associated secretion pathways is indicated on the right as

963 colored boxes. The scale bar represents the average number of substitutions per site. See also
964 **Supplementary Table 1** for detailed information.
965
966 **Supplementary Figure 3. Purification of the $Cpe1_{tox}$-Cpi1 complex and protein expression**
967 **levels of Cpi1 variants.** Related to **Figure 2. (a)** Coomassie-stained SDS-PAGE analysis of the
968 His-tagged $Cpe1_{tox}$ co-purified with Cpi1. **(b)** Protein expression levels of wild-type Cpi1 and
969 variants, as assessed by immunoblotting analysis. The cytosolic protein RpoB was used as a
970 loading control.
971
972 **Supplementary Figure 4. $ComA_{pep}$ and $LahT_{pep}$ feature hydrophobic concave regions on**
973 **their surfaces near the catalytic pocket.** Related to **Figure 3. (a, b)** Depiction of $ComA_{pep}$ **(a)**
974 and $LahT_{pep}$ **(b)** illustrating the location of their respective catalytic pockets and hydrophobic
975 concave surfaces. $ComA_{pep}$ (PDB: 3K8U, light gray). $LahT_{pep}$ (PDB: 6MPZ, dark gray).
976
977 **Supplementary Figure 5. $Cpe1_{tox}$ specifically targets and cleaves GyrB and ParE among eight**
978 **candidate substrates identified from the interactome analysis.** Related to **Figure 3. (a-f)**
979 Coomassie-stained SDS-PAGE analysis of the *in vitro* cleavage assay of six candidate substrates
980 of $Cpe1_{tox}$: AccA **(a)**, DapE **(b)**, FtsZ **(c)**, NusA **(d)**, NusG **(e)**, and RpoB **(f)**. **(g, h)** Presence of
981 Cpi1 suppressed the cleavage of GyrB **(g)** and ParE **(h)** by $Cpe1_{tox}$. The substrates were incubated
982 with $Cpe1_{tox}$ (lanes 1 and 2), $Cpe1_{tox}^{C362A}$ (lanes 3 and 4), or $Cpe1_{tox}$ and Cpi1 (lanes 5 and 6).
983 Cleaved fragments are indicated with red arrowheads.
984

985 **Supplementary Figure 6. Cleavage sequences of ComA and LahT and mass spectrometric**
986 **analysis of Cpe1-cleaved fragments.** Related to **Figure 4. (a, b)** Sequence logos showing the
987 consensus sequence recognized by ComA **(a)** and LahT **(b)**. **(c, d)** Mapping of peptide sequences
988 from $Cpe1_{tox}$-digested GyrB **(c)** and ParE **(d)** fragments. $Cpe1_{tox}$-cleaved fragments, resolved by
989 Coomassie-stained SDS-PAGE, were purified, trypsin-digested, and subjected to MALDI-TOF
990 analysis. The intensity of the signals (Y-axis) from identified peptides and their coverage across
991 the respective full-length protein (X-axis) are plotted below. Upper chart: peptides from the small
992 fragment. Lower chart: peptides from the large fragment.
993
994 **Supplementary Figure 7. Cpe1 intoxication inhibits chromosome segregation in *E. coli*.**
995 Related to **Figure 4f. (a)** Phase-contrast (top), blue fluorescence (middle), and merged (bottom)
996 images of *E. coli* carrying an empty vector, *E. coli* expressing $Cpe1_{tox}$, *E. coli* expressing
997 $Cpe1_{tox}^{C362A}$, or *E. coli* co-expressing $Cpe1_{tox}$ and Cpi1, after three hours of induction. Scale bar =
998 20 μm. The white borders demarcate the cropped images displayed in **Figure 4f**.
999
1000 **Supplementary Figure 8. Z-ring formation is disrupted in Cpe1-intoxicated *E. coli*.** Related
1001 to **Figure 4f. (a)** Phase-contrast (top), blue fluorescence (second from top), green fluorescence
1002 (third from top), and merged (bottom) images of *E. coli* carrying an empty vector, shown before
1003 and after 2-hour incubation. **(b)** Fluorescence micrographs of *E. coli* intoxicated by $Cpe1_{tox}$. Phase-
1004 contrast (top), blue fluorescence (second from top), green fluorescence (third from top), and
1005 merged (bottom) images are presented. White borders indicate the zoomed-in regions shown in the
1006 bottom-right corner of each image. Scale bar = 20 μm.
1007

1008 **Supplementary Figure 9. Interactions between $Cpe1_{tox}$ with the substrates and kinetics of**
1009 **$Cpe1_{tox}$ with $Cpi1^{mut4}$.** Related to **Figures 5 a, e, f. (a, b)** Predicted assigned error (PAE) plots for
1010 the models of the $Cpe1_{tox}$-$GyrB_{ATPase}$ interaction **(a)** and the $Cpe1_{tox}$-$ParE_{ATPase}$ interaction **(b)** in
1011 **Figure 5a**. Accuracy of the predicted relative positions of subunits within the complex, as indicated
1012 by AlphaFold 3 prediction scores (iPTM). Confidence in the overall folding of the complex is
1013 indicated by pTM scores. **(c)** Predicted structure of $Cpe1_{tox}$-$GyrB_{ATPase}$ interaction, showing the
1014 entrance of the consensus loop of GyrB into the active site of Cpe1 (left panel). The magnified
1015 view of the active pocket (right panel) implies possible catalysis. **(d)** $Cpe1_{tox}$ targets the ATPase
1016 domain of ParE. Cleavage of full-length ParE and the ATPase domain by $Cpe1_{tox}$ was analyzed by
1017 Coomassie-stained SDS-PAGE. Cleaved fragments are indicated with red arrowheads. **(e)** Results
1018 of kinetic assays on interactions between $Cpi1^{mut4}$ and $Cpe1_{tox}^{C362A}$ using biolayer interferometry
1019 (BLI). Data from three replicates have been plotted on an X-Y scatter graph. The Y-axis represents
1020 wavelength shift (nm) generated by binding of the two proteins, which is nearly non-detectable
1021 (N.D.). The X-axis represents reaction time in seconds. A vertical dashed line marks the transition
1022 from the association step to the dissociation step. Kinetic parameters such as K_d, K_{on}, K_{off}, and
1023 Rmax could not be calculated and are labeled as ND.
1024
1025 **Video 1. Time-lapse phase contrast microscopy series of *E. coli* containing an empty vector.**
1026 Related to **Figure 2.**
1027
1028 **Video 2. Time-lapse phase contrast microscopy series of *E. coli* expressing $Cpe1_{tox}$.** Related to
1029 **Figure 2.**
1030

1031 **Video 3. Time-lapse phase contrast microscopy series of *E. coli* expressing Cpe1$_{tox}^{C362A}$.**
1032 Related to **Figure 2.**
1033
1034 **Video 4. Time-lapse phase contrast microscopy series of *E. coli* co-expressing Cpe1$_{tox}$ and**
1035 **Cpi1.** Related to **Figure 2.**
1036
1037 **Supplementary Table 1. Identified interbacterial PLCP effectors and their putative cognate**
1038 **immunity proteins.** Relevant to **Figure 1**, **Supplementary Figure 1**, and **Supplementary Figure**
1039 **2**.
1040
1041 **Supplementary Table 2. X-ray data collection and refinement statistics.** Relevant to **Methods**
1042 and **Figure 2**.
1043
1044 **Supplementary Table 3. The interactome of Cpe1 identified by Bpa-crosslinking and LC-**
1045 **MS/MS analysis.** Relevant to **Figure 3**.
1046
1047 **Supplementary Table 4. Strains, recombinant DNA, and oligonucleotides used in this stud**y.
1048

1049 ## Author Contributions

1050 P.-Y.S., C.-E.T., C.K., K.-C.H., and S.-Y.T. designed the study. P.-Y.S., C.-E.T., Y.-C.C., P.-P.C.,
1051 T.-H.W., P.-Y.C., and C.-Y.H. performed experiments. P.-Y.S., C.-E.T., P.-P.C., K.-C.H., and S.-
1052 Y.T. analyzed data. P.-Y.S., C.-E.T., Y.-C.C., P.-P.C., P.-Y.C., K.-C.H., and S.-Y.T. wrote the
1053 manuscript.

1054 **References**

1055 1. Raaijmakers, J.M., and Mazzola, M. (2012). Diversity and natural functions of antibiotics
1056 produced by beneficial and plant pathogenic bacteria. Annu Rev Phytopathol *50*, 403-424.
1057 10.1146/annurev-phyto-081211-172908.
1058 2. Riley, M.A., and Wertz, J.E. (2002). Bacteriocins: evolution, ecology, and application. Annu
1059 Rev Microbiol *56*, 117-137. 10.1146/annurev.micro.56.012302.161024.
1060 3. Aoki, S.K., Pamma, R., Hernday, A.D., Bickham, J.E., Braaten, B.A., and Low, D.A. (2005).
1061 Contact-dependent inhibition of growth in Escherichia coli. Science *309*, 1245-1248.
1062 10.1126/science.1115109.
1063 4. Cao, Z., Casabona, M.G., Kneuper, H., Chalmers, J.D., and Palmer, T. (2016). The type VII
1064 secretion system of Staphylococcus aureus secretes a nuclease toxin that targets
1065 competitor bacteria. Nat Microbiol *2*, 16183. 10.1038/nmicrobiol.2016.183.
1066 5. Hood, R.D., Singh, P., Hsu, F., Guvener, T., Carl, M.A., Trinidad, R.R., Silverman, J.M., Ohlson,
1067 B.B., Hicks, K.G., Plemel, R.L., et al. (2010). A type VI secretion system of Pseudomonas
1068 aeruginosa targets a toxin to bacteria. Cell Host Microbe *7*, 25-37.
1069 10.1016/j.chom.2009.12.007.
1070 6. Jamet, A., Jousset, A.B., Euphrasie, D., Mukorako, P., Boucharlat, A., Ducousso, A., Charbit,
1071 A., and Nassif, X. (2015). A new family of secreted toxins in pathogenic Neisseria species.
1072 PLoS Pathog *11*, e1004592. 10.1371/journal.ppat.1004592.
1073 7. Souza, D.P., Oka, G.U., Alvarez-Martinez, C.E., Bisson-Filho, A.W., Dunger, G., Hobeika, L.,
1074 Cavalcante, N.S., Alegria, M.C., Barbosa, L.R., Salinas, R.K., et al. (2015). Bacterial killing
1075 via a type IV secretion system. Nat Commun *6*, 6453. 10.1038/ncomms7453.
1076 8. Vassallo, C.N., Cao, P., Conklin, A., Finkelstein, H., Hayes, C.S., and Wall, D. (2017).
1077 Infectious polymorphic toxins delivered by outer membrane exchange discriminate kin in
1078 myxobacteria. Elife *6*. 10.7554/eLife.29397.
1079 9. Whitney, J.C., Peterson, S.B., Kim, J., Pazos, M., Verster, A.J., Radey, M.C., Kulasekara, H.D.,
1080 Ching, M.Q., Bullen, N.P., Bryant, D., et al. (2017). A broadly distributed toxin family
1081 mediates contact-dependent antagonism between gram-positive bacteria. Elife *6*.
1082 10.7554/eLife.26938.
1083 10. Sana, T.G., Flaugnatti, N., Lugo, K.A., Lam, L.H., Jacobson, A., Baylot, V., Durand, E., Journet,
1084 L., Cascales, E., and Monack, D.M. (2016). Salmonella Typhimurium utilizes a T6SS-
1085 mediated antibacterial weapon to establish in the host gut. Proc Natl Acad Sci U S A *113*,
1086 E5044-5051. 10.1073/pnas.1608858113.
1087 11. Speare, L., Cecere, A.G., Guckes, K.R., Smith, S., Wollenberg, M.S., Mandel, M.J., Miyashiro,
1088 T., and Septer, A.N. (2018). Bacterial symbionts use a type VI secretion system to eliminate
1089 competitors in their natural host. Proc Natl Acad Sci U S A *115*, E8528-E8537.
1090 10.1073/pnas.1808302115.
1091 12. Verster, A.J., Ross, B.D., Radey, M.C., Bao, Y., Goodman, A.L., Mougous, J.D., and
1092 Borenstein, E. (2017). The Landscape of Type VI Secretion across Human Gut Microbiomes
1093 Reveals Its Role in Community Composition. Cell Host Microbe *22*, 411-419 e414.
1094 10.1016/j.chom.2017.08.010.
1095 13. Russell, A.B., Hood, R.D., Bui, N.K., LeRoux, M., Vollmer, W., and Mougous, J.D. (2011).
1096 Type VI secretion delivers bacteriolytic effectors to target cells. Nature *475*, 343-347.
1097 10.1038/nature10244.

1098 14. Russell, A.B., LeRoux, M., Hathazi, K., Agnello, D.M., Ishikawa, T., Wiggins, P.A., Wai, S.N.,
1099 and Mougous, J.D. (2013). Diverse type VI secretion phospholipases are functionally
1100 plastic antibacterial effectors. Nature *496*, 508-512. 10.1038/nature12074.
1101 15. Fridman, C.M., Keppel, K., Gerlic, M., Bosis, E., and Salomon, D. (2020). A comparative
1102 genomics methodology reveals a widespread family of membrane-disrupting T6SS
1103 effectors. Nat Commun *11*, 1085. 10.1038/s41467-020-14951-4.
1104 16. Sibinelli-Sousa, S., Hespanhol, J.T., Nicastro, G.G., Matsuyama, B.Y., Mesnage, S., Patel, A.,
1105 de Souza, R.F., Guzzo, C.R., and Bayer-Santos, E. (2020). A Family of T6SS Antibacterial
1106 Effectors Related to l,d-Transpeptidases Targets the Peptidoglycan. Cell Rep *31*, 107813.
1107 10.1016/j.celrep.2020.107813.
1108 17. Le, N.H., Pinedo, V., Lopez, J., Cava, F., and Feldman, M.F. (2021). Killing of Gram-negative
1109 and Gram-positive bacteria by a bifunctional cell wall-targeting T6SS effector. Proc Natl
1110 Acad Sci U S A *118*. 10.1073/pnas.2106555118.
1111 18. LaCourse, K.D., Peterson, S.B., Kulasekara, H.D., Radey, M.C., Kim, J., and Mougous, J.D.
1112 (2018). Conditional toxicity and synergy drive diversity among antibacterial effectors. Nat
1113 Microbiol *3*, 440-446. 10.1038/s41564-018-0113-y.
1114 19. Mariano, G., Trunk, K., Williams, D.J., Monlezun, L., Strahl, H., Pitt, S.J., and Coulthurst, S.J.
1115 (2019). A family of Type VI secretion system effector proteins that form ion-selective pores.
1116 Nat Commun *10*, 5484. 10.1038/s41467-019-13439-0.
1117 20. Halvorsen, T.M., Schroeder, K.A., Jones, A.M., Hammarlof, D., Low, D.A., Koskiniemi, S.,
1118 and Hayes, C.S. (2024). Contact-dependent growth inhibition (CDI) systems deploy a large
1119 family of polymorphic ionophoric toxins for inter-bacterial competition. PLoS Genet *20*,
1120 e1011494. 10.1371/journal.pgen.1011494.
1121 21. Ma, L.S., Hachani, A., Lin, J.S., Filloux, A., and Lai, E.M. (2014). Agrobacterium tumefaciens
1122 deploys a superfamily of type VI secretion DNase effectors as weapons for interbacterial
1123 competition in planta. Cell Host Microbe *16*, 94-104. 10.1016/j.chom.2014.06.002.
1124 22. Whitney, J.C., Quentin, D., Sawai, S., LeRoux, M., Harding, B.N., Ledvina, H.E., Tran, B.Q.,
1125 Robinson, H., Goo, Y.A., Goodlett, D.R., et al. (2015). An interbacterial NAD(P)(+)
1126 glycohydrolase toxin requires elongation factor Tu for delivery to target cells. Cell *163*,
1127 607-619. 10.1016/j.cell.2015.09.027.
1128 23. Ahmad, S., Wang, B., Walker, M.D., Tran, H.R., Stogios, P.J., Savchenko, A., Grant, R.A.,
1129 McArthur, A.G., Laub, M.T., and Whitney, J.C. (2019). An interbacterial toxin inhibits target
1130 cell growth by synthesizing (p)ppApp. Nature *575*, 674-678. 10.1038/s41586-019-1735-9.
1131 24. Mok, B.Y., de Moraes, M.H., Zeng, J., Bosch, D.E., Kotrys, A.V., Raguram, A., Hsu, F., Radey,
1132 M.C., Peterson, S.B., Mootha, V.K., et al. (2020). A bacterial cytidine deaminase toxin
1133 enables CRISPR-free mitochondrial base editing. Nature *583*, 631-637. 10.1038/s41586-
1134 020-2477-4.
1135 25. Bullen, N.P., Sychantha, D., Thang, S.S., Culviner, P.H., Rudzite, M., Ahmad, S., Shah, V.S.,
1136 Filloux, A., Prehna, G., and Whitney, J.C. (2022). An ADP-ribosyltransferase toxin kills
1137 bacterial cells by modifying structured non-coding RNAs. Mol Cell *82*, 3484-3498 e3411.
1138 10.1016/j.molcel.2022.08.015.
1139 26. Aoki, S.K., Diner, E.J., de Roodenbeke, C.T., Burgess, B.R., Poole, S.J., Braaten, B.A., Jones,
1140 A.M., Webb, J.S., Hayes, C.S., Cotter, P.A., and Low, D.A. (2010). A widespread family of

1141 polymorphic contact-dependent toxin delivery systems in bacteria. Nature *468*, 439-442.
1142 10.1038/nature09490.
1143 27. Ting, S.Y., Bosch, D.E., Mangiameli, S.M., Radey, M.C., Huang, S., Park, Y.J., Kelly, K.A., Filip,
1144 S.K., Goo, Y.A., Eng, J.K., et al. (2018). Bifunctional Immunity Proteins Protect Bacteria
1145 against FtsZ-Targeting ADP-Ribosylating Toxins. Cell *175*, 1380-1392 e1314.
1146 10.1016/j.cell.2018.09.037.
1147 28. Wang, D., Zhu, L., Zhen, X., Yang, D., Li, C., Chen, Y., Wang, H., Qu, Y., Liu, X., Yin, Y., et al.
1148 (2022). A secreted effector with a dual role as a toxin and as a transcriptional factor. Nat
1149 Commun *13*, 7779. 10.1038/s41467-022-35522-9.
1150 29. Jurenas, D., Rey, M., Byrne, D., Chamot-Rooke, J., Terradot, L., and Cascales, E. (2022).
1151 Salmonella antibacterial Rhs polymorphic toxin inhibits translation through ADP-
1152 ribosylation of EF-Tu P-loop. Nucleic Acids Res *50*, 13114-13127. 10.1093/nar/gkac1162.
1153 30. Dumont, B., Terradot, L., Cascales, E., Van Melderen, L., and Jurenas, D. (2024).
1154 Thioredoxin 1 moonlights as a chaperone for an interbacterial ADP-ribosyltransferase
1155 toxin. Nat Commun *15*, 10388. 10.1038/s41467-024-54892-w.
1156 31. Alcoforado Diniz, J., Liu, Y.C., and Coulthurst, S.J. (2015). Molecular weaponry: diverse
1157 effectors delivered by the Type VI secretion system. Cell Microbiol *17*, 1742-1751.
1158 10.1111/cmi.12532.
1159 32. Bosch, D.E., Abbasian, R., Parajuli, B., Peterson, S.B., and Mougous, J.D. (2023). Structural
1160 disruption of Ntox15 nuclease effector domains by immunity proteins protects against
1161 type VI secretion system intoxication in Bacteroidales. mBio *14*, e0103923.
1162 10.1128/mbio.01039-23.
1163 33. Zhang, D., de Souza, R.F., Anantharaman, V., Iyer, L.M., and Aravind, L. (2012). Polymorphic
1164 toxin systems: Comprehensive characterization of trafficking modes, processing,
1165 mechanisms of action, immunity and ecology using comparative genomics. Biol Direct *7*,
1166 18. 10.1186/1745-6150-7-18.
1167 34. Nachmias, N., Dotan, N., Rocha, M.C., Fraenkel, R., Detert, K., Kluzek, M., Shalom, M.,
1168 Cheskis, S., Peedikayil-Kurien, S., Meitav, G., et al. (2024). Systematic discovery of
1169 antibacterial and antifungal bacterial toxins. Nat Microbiol *9*, 3041-3058.
1170 10.1038/s41564-024-01820-9.
1171 35. Geller, A.M., Shalom, M., Zlotkin, D., Blum, N., and Levy, A. (2024). Identification of type
1172 VI secretion system effector-immunity pairs using structural bioinformatics. Mol Syst Biol
1173 *20*, 702-718. 10.1038/s44320-024-00035-8.
1174 36. Li, D.Y., Liu, Y.L., Liao, X.J., He, T.T., Sun, S.S., Nie, P., and Xie, H.X. (2021). Identification and
1175 Characterization of EvpQ, a Novel T6SS Effector Encoded on a Mobile Genetic Element in
1176 Edwardsiella piscicida. Front Microbiol *12*, 643498. 10.3389/fmicb.2021.643498.
1177 37. Lu, W., Lu, H., Wang, C., Wang, G., Dong, W., and Tan, C. (2023). Effectors of the Type VI
1178 Secretion System Have the Potential to Be Modified into Antimicrobial Peptides. Microbiol
1179 Spectr *11*, e0030823. 10.1128/spectrum.00308-23.
1180 38. Wood, T.E., Howard, S.A., Forster, A., Nolan, L.M., Manoli, E., Bullen, N.P., Yau, H.C.L.,
1181 Hachani, A., Hayward, R.D., Whitney, J.C., et al. (2019). The Pseudomonas aeruginosa T6SS
1182 Delivers a Periplasmic Toxin that Disrupts Bacterial Cell Morphology. Cell Rep *29*, 187-201
1183 e187. 10.1016/j.celrep.2019.08.094.

1184 39. Ashida, H., Sasakawa, C., and Suzuki, T. (2020). A unique bacterial tactic to circumvent the
1185 cell death crosstalk induced by blockade of caspase-8. EMBO J *39*, e104469.
1186 10.15252/embj.2020104469.
1187 40. Gavin, H.E., Beubier, N.T., and Satchell, K.J. (2017). The Effector Domain Region of the
1188 Vibrio vulnificus MARTX Toxin Confers Biphasic Epithelial Barrier Disruption and Is
1189 Essential for Systemic Spread from the Intestine. PLoS Pathog *13*, e1006119.
1190 10.1371/journal.ppat.1006119.
1191 41. Kitadokoro, K., Kamitani, S., Miyazawa, M., Hanajima-Ozawa, M., Fukui, A., Miyake, M.,
1192 and Horiguchi, Y. (2007). Crystal structures reveal a thiol protease-like catalytic triad in the
1193 C-terminal region of Pasteurella multocida toxin. Proc Natl Acad Sci U S A *104*, 5139-5144.
1194 10.1073/pnas.0608197104.
1195 42. Havarstein, L.S., Diep, D.B., and Nes, I.F. (1995). A family of bacteriocin ABC transporters
1196 carry out proteolytic processing of their substrates concomitant with export. Mol
1197 Microbiol *16*, 229-240. 10.1111/j.1365-2958.1995.tb02295.x.
1198 43. Kanonenberg, K., Spitz, O., Erenburg, I.N., Beer, T., and Schmitt, L. (2018). Type I secretion
1199 system-it takes three and a substrate. FEMS Microbiol Lett *365*. 10.1093/femsle/fny094.
1200 44. Kieuvongngam, V., Olinares, P.D.B., Palillo, A., Oldham, M.L., Chait, B.T., and Chen, J. (2020).
1201 Structural basis of substrate recognition by a polypeptide processing and secretion
1202 transporter. Elife *9*. 10.7554/eLife.51492.
1203 45. Altschul, S.F., Madden, T.L., Schaffer, A.A., Zhang, J., Zhang, Z., Miller, W., and Lipman, D.J.
1204 (1997). Gapped BLAST and PSI-BLAST: a new generation of protein database search
1205 programs. Nucleic Acids Res *25*, 3389-3402. 10.1093/nar/25.17.3389.
1206 46. Jurenas, D., and Journet, L. (2021). Activity, delivery, and diversity of Type VI secretion
1207 effectors. Mol Microbiol *115*, 383-394. 10.1111/mmi.14648.
1208 47. Gunther, P., Quentin, D., Ahmad, S., Sachar, K., Gatsogiannis, C., Whitney, J.C., and Raunser,
1209 S. (2022). Structure of a bacterial Rhs effector exported by the type VI secretion system.
1210 PLoS Pathog *18*, e1010182. 10.1371/journal.ppat.1010182.
1211 48. Klein, T.A., Ahmad, S., and Whitney, J.C. (2020). Contact-Dependent Interbacterial
1212 Antagonism Mediated by Protein Secretion Machines. Trends Microbiol *28*, 387-400.
1213 10.1016/j.tim.2020.01.003.
1214 49. Ishii, S., Yano, T., and Hayashi, H. (2006). Expression and characterization of the peptidase
1215 domain of Streptococcus pneumoniae ComA, a bifunctional ATP-binding cassette
1216 transporter involved in quorum sensing pathway. J Biol Chem *281*, 4726-4731.
1217 10.1074/jbc.M512516200.
1218 50. Bobeica, S.C., Dong, S.H., Huo, L., Mazo, N., McLaughlin, M.I., Jimenez-Oses, G., Nair, S.K.,
1219 and van der Donk, W.A. (2019). Insights into AMS/PCAT transporters from biochemical and
1220 structural characterization of a double Glycine motif protease. Elife *8*.
1221 10.7554/eLife.42305.
1222 51. Ozhelvaci, F., and Steczkiewicz, K. (2023). Identification and classification of papain-like
1223 cysteine proteinases. J Biol Chem *299*, 104801. 10.1016/j.jbc.2023.104801.
1224 52. Ishii, S., Yano, T., Ebihara, A., Okamoto, A., Manzoku, M., and Hayashi, H. (2010). Crystal
1225 structure of the peptidase domain of Streptococcus ComA, a bifunctional ATP-binding
1226 cassette transporter involved in the quorum-sensing pathway. J Biol Chem *285*, 10777-
1227 10785. 10.1074/jbc.M109.093781.

1228 53. Holm, L. (2022). Dali server: structural unification of protein families. Nucleic Acids Res *50*,
1229 W210-W215. 10.1093/nar/gkac387.
1230 54. Ishii, S., Fukui, K., Yokoshima, S., Kumagai, K., Beniyama, Y., Kodama, T., Fukuyama, T.,
1231 Okabe, T., Nagano, T., Kojima, H., and Yano, T. (2017). High-throughput Screening of Small
1232 Molecule Inhibitors of the Streptococcus Quorum-sensing Signal Pathway. Sci Rep *7*, 4029.
1233 10.1038/s41598-017-03567-2.
1234 55. Chin, J.W., Martin, A.B., King, D.S., Wang, L., and Schultz, P.G. (2002). Addition of a
1235 photocrosslinking amino acid to the genetic code of Escherichiacoli. Proc Natl Acad Sci U
1236 S A *99*, 11020-11024. 10.1073/pnas.172226299.
1237 56. Kauer, J.C., Erickson-Viitanen, S., Wolfe, H.R., Jr., and DeGrado, W.F. (1986). p-Benzoyl-L-
1238 phenylalanine, a new photoreactive amino acid. Photolabeling of calmodulin with a
1239 synthetic calmodulin-binding peptide. J Biol Chem *261*, 10695-10700.
1240 57. Karp, P.D., Weaver, D., Paley, S., Fulcher, C., Kubo, A., Kothari, A., Krummenacker, M.,
1241 Subhraveti, P., Weerasinghe, D., Gama-Castro, S., et al. (2014). The EcoCyc Database.
1242 EcoSal Plus *6*. 10.1128/ecosalplus.ESP-0009-2013.
1243 58. Baba, T., Ara, T., Hasegawa, M., Takai, Y., Okumura, Y., Baba, M., Datsenko, K.A., Tomita,
1244 M., Wanner, B.L., and Mori, H. (2006). Construction of Escherichia coli K-12 in-frame,
1245 single-gene knockout mutants: the Keio collection. Mol Syst Biol *2*, 2006 0008.
1246 10.1038/msb4100050.
1247 59. Havarstein, L.S., Holo, H., and Nes, I.F. (1994). The leader peptide of colicin V shares
1248 consensus sequences with leader peptides that are common among peptide bacteriocins
1249 produced by gram-positive bacteria. Microbiology (Reading) *140 (Pt 9)*, 2383-2389.
1250 10.1099/13500872-140-9-2383.
1251 60. Kotake, Y., Ishii, S., Yano, T., Katsuoka, Y., and Hayashi, H. (2008). Substrate recognition
1252 mechanism of the peptidase domain of the quorum-sensing-signal-producing ABC
1253 transporter ComA from Streptococcus. Biochemistry *47*, 2531-2538. 10.1021/bi702253n.
1254 61. Levine, C., Hiasa, H., and Marians, K.J. (1998). DNA gyrase and topoisomerase IV:
1255 biochemical activities, physiological roles during chromosome replication, and drug
1256 sensitivities. Biochim Biophys Acta *1400*, 29-43. 10.1016/s0167-4781(98)00126-2.
1257 62. Bush, N.G., Evans-Roberts, K., and Maxwell, A. (2015). DNA Topoisomerases. EcoSal Plus
1258 *6*. 10.1128/ecosalplus.ESP-0010-2014.
1259 63. Wang, J.C. (2002). Cellular roles of DNA topoisomerases: a molecular perspective. Nat Rev
1260 Mol Cell Biol *3*, 430-440. 10.1038/nrm831.
1261 64. Drlica, K., and Zhao, X. (1997). DNA gyrase, topoisomerase IV, and the 4-quinolones.
1262 Microbiol Mol Biol Rev *61*, 377-392. 10.1128/mmbr.61.3.377-392.1997.
1263 65. Azam, M.A., Thathan, J., and Jubie, S. (2015). Dual targeting DNA gyrase B (GyrB) and
1264 topoisomerse IV (ParE) inhibitors: A review. Bioorg Chem *62*, 41-63.
1265 10.1016/j.bioorg.2015.07.004.
1266 66. Vanden Broeck, A., Lotz, C., Ortiz, J., and Lamour, V. (2019). Cryo-EM structure of the
1267 complete E. coli DNA gyrase nucleoprotein complex. Nat Commun *10*, 4935.
1268 10.1038/s41467-019-12914-y.
1269 67. Bellon, S., Parsons, J.D., Wei, Y., Hayakawa, K., Swenson, L.L., Charifson, P.S., Lippke, J.A.,
1270 Aldape, R., and Gross, C.H. (2004). Crystal structures of Escherichia coli topoisomerase IV
1271 ParE subunit (24 and 43 kilodaltons): a single residue dictates differences in novobiocin

1272 potency against topoisomerase IV and DNA gyrase. Antimicrob Agents Chemother *48*,
1273 1856-1864. 10.1128/AAC.48.5.1856-1864.2004.
1274 68. Caron, P.R., and Wang, J.C. (1994). Appendix. II: Alignment of primary sequences of DNA
1275 topoisomerases. Adv Pharmacol *29B*, 271-297. 10.1016/s1054-3589(08)61143-6.
1276 69. O'Dea, M.H., Tamura, J.K., and Gellert, M. (1996). Mutations in the B subunit of
1277 Escherichia coli DNA gyrase that affect ATP-dependent reactions. J Biol Chem *271*, 9723-
1278 9729. 10.1074/jbc.271.16.9723.
1279 70. Lamour, V., Hoermann, L., Jeltsch, J.M., Oudet, P., and Moras, D. (2002). An open
1280 conformation of the Thermus thermophilus gyrase B ATP-binding domain. J Biol Chem *277*,
1281 18947-18953. 10.1074/jbc.M111740200.
1282 71. Clark, D.J., and Leblanc, B. (2009). Analysis of DNA supercoiling induced by DNA-protein
1283 interactions. Methods Mol Biol *543*, 523-535. 10.1007/978-1-60327-015-1_30.
1284 72. Lockshon, D., and Morris, D.R. (1983). Positively supercoiled plasmid DNA is produced by
1285 treatment of Escherichia coli with DNA gyrase inhibitors. Nucleic Acids Res *11*, 2999-3017.
1286 10.1093/nar/11.10.2999.
1287 73. Mossessova, E., Levine, C., Peng, H., Nurse, P., Bahng, S., and Marians, K.J. (2000).
1288 Mutational analysis of Escherichia coli topoisomerase IV. I. Selection of dominant-negative
1289 parE alleles. J Biol Chem *275*, 4099-4103. 10.1074/jbc.275.6.4099.
1290 74. Kato, J., Nishimura, Y., Imamura, R., Niki, H., Hiraga, S., and Suzuki, H. (1990). New
1291 topoisomerase essential for chromosome segregation in E. coli. Cell *63*, 393-404.
1292 10.1016/0092-8674(90)90172-b.
1293 75. Smith, D.H., and Davis, B.D. (1967). Mode of action of novobiocin in Escherichia coli. J
1294 Bacteriol *93*, 71-79. 10.1128/jb.93.1.71-79.1967.
1295 76. Ouyang, X., Hoeksma, J., Lubbers, R.J.M., Siersma, T.K., Hamoen, L.W., and den Hertog, J.
1296 (2022). Classification of antimicrobial mechanism of action using dynamic bacterial
1297 morphology imaging. Sci Rep *12*, 11162. 10.1038/s41598-022-15405-1.
1298 77. Moore, D.A., Whatley, Z.N., Joshi, C.P., Osawa, M., and Erickson, H.P. (2017). Probing for
1299 Binding Regions of the FtsZ Protein Surface through Site-Directed Insertions: Discovery of
1300 Fully Functional FtsZ-Fluorescent Proteins. J Bacteriol *199*. 10.1128/JB.00553-16.
1301 78. Abramson, J., Adler, J., Dunger, J., Evans, R., Green, T., Pritzel, A., Ronneberger, O.,
1302 Willmore, L., Ballard, A.J., Bambrick, J., et al. (2024). Accurate structure prediction of
1303 biomolecular interactions with AlphaFold 3. Nature *630*, 493-500. 10.1038/s41586-024-
1304 07487-w.
1305 79. Shao, F., Merritt, P.M., Bao, Z., Innes, R.W., and Dixon, J.E. (2002). A Yersinia effector and a
1306 Pseudomonas avirulence protein define a family of cysteine proteases functioning in
1307 bacterial pathogenesis. Cell *109*, 575-588. 10.1016/s0092-8674(02)00766-3.
1308 80. Shao, F., Golstein, C., Ade, J., Stoutemyer, M., Dixon, J.E., and Innes, R.W. (2003). Cleavage
1309 of Arabidopsis PBS1 by a bacterial type III effector. Science *301*, 1230-1233.
1310 10.1126/science.1085671.
1311 81. Kourelis, J., van der Hoorn, R.A.L., and Sueldo, D.J. (2016). Decoy Engineering: The Next
1312 Step in Resistance Breeding. Trends Plant Sci *21*, 371-373. 10.1016/j.tplants.2016.04.001.
1313 82. Noeske-Jungblut, C., Haendler, B., Donner, P., Alagon, A., Possani, L., and Schleuning, W.D.
1314 (1995). Triabin, a highly potent exosite inhibitor of thrombin. J Biol Chem *270*, 28629-
1315 28634. 10.1074/jbc.270.48.28629.

1316 83. Fuentes-Prior, P., Noeske-Jungblut, C., Donner, P., Schleuning, W.D., Huber, R., and Bode,
1317 W. (1997). Structure of the thrombin complex with triabin, a lipocalin-like exosite-binding
1318 inhibitor derived from a triatomine bug. Proc Natl Acad Sci U S A *94*, 11845-11850.
1319 10.1073/pnas.94.22.11845.
1320 84. Hanna, R.A., Campbell, R.L., and Davies, P.L. (2008). Calcium-bound structure of calpain
1321 and its mechanism of inhibition by calpastatin. Nature *456*, 409-412.
1322 10.1038/nature07451.
1323 85. Moldoveanu, T., Gehring, K., and Green, D.R. (2008). Concerted multi-pronged attack by
1324 calpastatin to occlude the catalytic cleft of heterodimeric calpains. Nature *456*, 404-408.
1325 10.1038/nature07353.
1326 86. Kleanthous, C., and Walker, D. (2001). Immunity proteins: enzyme inhibitors that avoid the
1327 active site. Trends Biochem Sci *26*, 624-631. 10.1016/s0968-0004(01)01941-7.
1328 87. Schiavo, G., and van der Goot, F.G. (2001). The bacterial toxin toolkit. Nat Rev Mol Cell Biol
1329 *2*, 530-537. 10.1038/35080089.
1330 88. Schiavo, G., Benfenati, F., Poulain, B., Rossetto, O., Polverino de Laureto, P., DasGupta, B.R.,
1331 and Montecucco, C. (1992). Tetanus and botulinum-B neurotoxins block neurotransmitter
1332 release by proteolytic cleavage of synaptobrevin. Nature *359*, 832-835.
1333 10.1038/359832a0.
1334 89. Sutormin, D.A., Galivondzhyan, A.K., Polkhovskiy, A.V., Kamalyan, S.O., Severinov, K.V., and
1335 Dubiley, S.A. (2021). Diversity and Functions of Type II Topoisomerases. Acta Naturae *13*,
1336 59-75. 10.32607/actanaturae.11058.
1337 90. Wang, J., Chitsaz, F., Derbyshire, M.K., Gonzales, N.R., Gwadz, M., Lu, S., Marchler, G.H.,
1338 Song, J.S., Thanki, N., Yamashita, R.A., et al. (2023). The conserved domain database in
1339 2023. Nucleic Acids Res *51*, D384-D388. 10.1093/nar/gkac1096.
1340 91. Journet, L., and Cascales, E. (2016). The Type VI Secretion System in Escherichia coli and
1341 Related Species. EcoSal Plus *7*. 10.1128/ecosalplus.ESP-0009-2015.
1342 92. Jones, A.M., Low, D.A., and Hayes, C.S. (2017). Can't you hear me knocking: contact-
1343 dependent competition and cooperation in bacteria. Emerg Top Life Sci *1*, 75-83.
1344 10.1042/ETLS20160019.
1345 93. Thompson, J.D., Higgins, D.G., and Gibson, T.J. (1994). CLUSTAL W: improving the
1346 sensitivity of progressive multiple sequence alignment through sequence weighting,
1347 position-specific gap penalties and weight matrix choice. Nucleic Acids Res *22*, 4673-4680.
1348 10.1093/nar/22.22.4673.
1349 94. Trifinopoulos, J., Nguyen, L.T., von Haeseler, A., and Minh, B.Q. (2016). W-IQ-TREE: a fast
1350 online phylogenetic tool for maximum likelihood analysis. Nucleic Acids Res *44*, W232-235.
1351 10.1093/nar/gkw256.
1352 95. Edwards, R.A., Keller, L.H., and Schifferli, D.M. (1998). Improved allelic exchange vectors
1353 and their use to analyze 987P fimbria gene expression. Gene *207*, 149-157.
1354 10.1016/s0378-1119(97)00619-7.
1355 96. Gibson, D.G., Young, L., Chuang, R.Y., Venter, J.C., Hutchison, C.A., 3rd, and Smith, H.O.
1356 (2009). Enzymatic assembly of DNA molecules up to several hundred kilobases. Nat
1357 Methods *6*, 343-345. 10.1038/nmeth.1318.

1358 97. Choi, K.H., Gaynor, J.B., White, K.G., Lopez, C., Bosio, C.M., Karkhoff-Schweizer, R.R., and
1359 Schweizer, H.P. (2005). A Tn7-based broad-range bacterial cloning and expression system.
1360 Nat Methods *2*, 443-448. 10.1038/nmeth765.
1361 98. Gross, C.H., Parsons, J.D., Grossman, T.H., Charifson, P.S., Bellon, S., Jernee, J., Dwyer, M.,
1362 Chambers, S.P., Markland, W., Botfield, M., and Raybuck, S.A. (2003). Active-site residues
1363 of Escherichia coli DNA gyrase required in coupling ATP hydrolysis to DNA supercoiling and
1364 amino acid substitutions leading to novobiocin resistance. Antimicrob Agents Chemother
1365 *47*, 1037-1046. 10.1128/AAC.47.3.1037-1046.2003.
1366 99. Wan, B., Zhang, Q., Ni, J., Li, S., Wen, D., Li, J., Xiao, H., He, P., Ou, H.Y., Tao, J., et al. (2017).
1367 Type VI secretion system contributes to Enterohemorrhagic Escherichia coli virulence by
1368 secreting catalase against host reactive oxygen species (ROS). PLoS Pathog *13*, e1006246.
1369 10.1371/journal.ppat.1006246.
1370 100. Brunet, Y.R., Khodr, A., Logger, L., Aussel, L., Mignot, T., Rimsky, S., and Cascales, E. (2015).
1371 H-NS Silencing of the Salmonella Pathogenicity Island 6-Encoded Type VI Secretion System
1372 Limits Salmonella enterica Serovar Typhimurium Interbacterial Killing. Infect Immun *83*,
1373 2738-2750. 10.1128/IAI.00198-15.
1374 101. Serapio-Palacios, A., Woodward, S.E., Vogt, S.L., Deng, W., Creus-Cuadros, A., Huus, K.E.,
1375 Cirstea, M., Gerrie, M., Barcik, W., Yu, H., and Finlay, B.B. (2022). Type VI secretion systems
1376 of pathogenic and commensal bacteria mediate niche occupancy in the gut. Cell Rep *39*,
1377 110731. 10.1016/j.celrep.2022.110731.
1378 102. Otwinowski, Z., and Minor, W. (1997). Processing of X-ray diffraction data collected in
1379 oscillation mode. Methods Enzymol *276*, 307-326. 10.1016/S0076-6879(97)76066-X.
1380 103. Adams, P.D., Afonine, P.V., Bunkoczi, G., Chen, V.B., Davis, I.W., Echols, N., Headd, J.J., Hung,
1381 L.W., Kapral, G.J., Grosse-Kunstleve, R.W., et al. (2010). PHENIX: a comprehensive Python-
1382 based system for macromolecular structure solution. Acta Crystallogr D Biol Crystallogr *66*,
1383 213-221. 10.1107/S0907444909052925.
1384 104. Emsley, P., and Cowtan, K. (2004). Coot: model-building tools for molecular graphics. Acta
1385 Crystallogr D Biol Crystallogr *60*, 2126-2132. 10.1107/S0907444904019158.
1386 105. Ryu, Y., and Schultz, P.G. (2006). Efficient incorporation of unnatural amino acids into
1387 proteins in Escherichia coli. Nat Methods *3*, 263-265. 10.1038/nmeth864.
1388 106. Cox, J., and Mann, M. (2008). MaxQuant enables high peptide identification rates,
1389 individualized p.p.b.-range mass accuracies and proteome-wide protein quantification.
1390 Nat Biotechnol *26*, 1367-1372. 10.1038/nbt.1511.
1391 107. Tyanova, S., Mann, M., and Cox, J. (2014). MaxQuant for in-depth analysis of large SILAC
1392 datasets. Methods Mol Biol *1188*, 351-364. 10.1007/978-1-4939-1142-4_24.
1393 108. Shevchenko, A., Tomas, H., Havlis, J., Olsen, J.V., and Mann, M. (2006). In-gel digestion for
1394 mass spectrometric characterization of proteins and proteomes. Nat Protoc *1*, 2856-2860.
1395 10.1038/nprot.2006.468.
1396 109. Liu, Y., Hua, Z.C., and Leng, F. (2018). DNA Supercoiling Measurement in Bacteria. Methods
1397 Mol Biol *1703*, 63-73. 10.1007/978-1-4939-7459-7_4.
1398 110. UniProt, C. (2023). UniProt: the Universal Protein Knowledgebase in 2023. Nucleic Acids
1399 Res *51*, D523-D531. 10.1093/nar/gkac1052.
1400 111. Crooks, G.E., Hon, G., Chandonia, J.M., and Brenner, S.E. (2004). WebLogo: a sequence
1401 logo generator. Genome Res *14*, 1188-1190. 10.1101/gr.849004.

1402

Figure 1

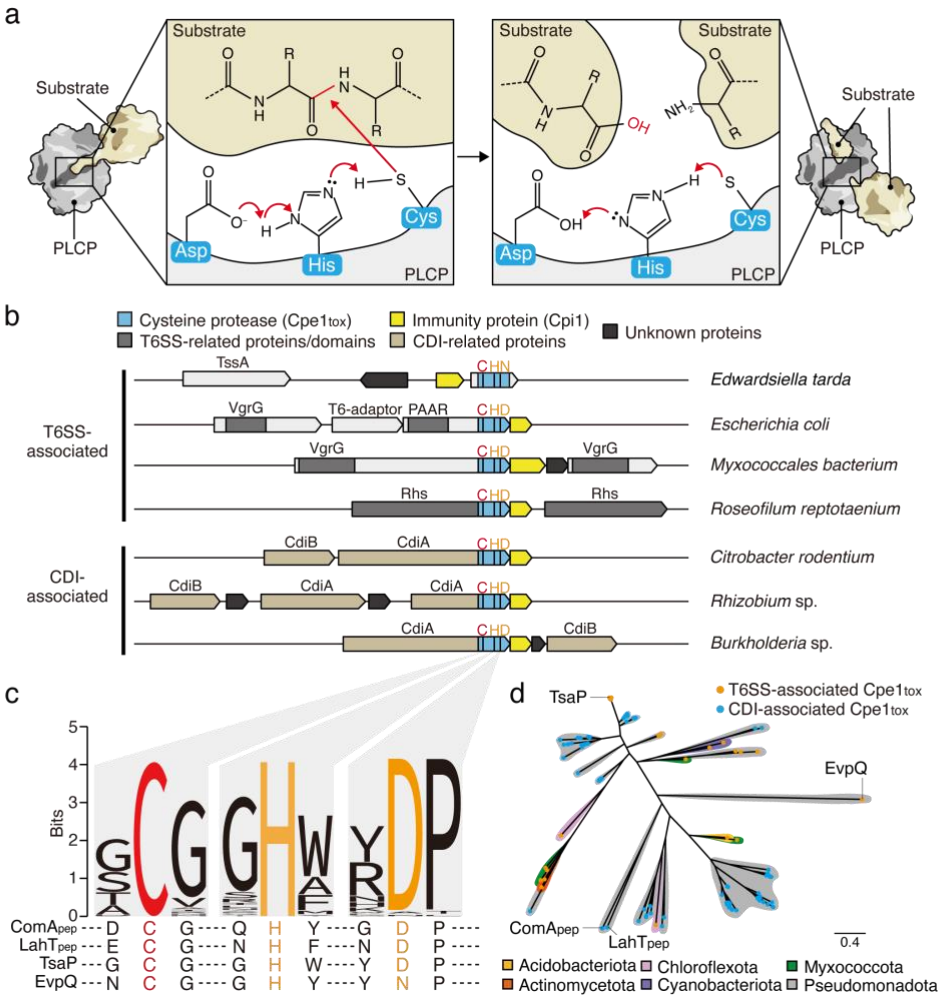

Figure 1. PLCP toxins are found in distinct Gram-negative species and are associated with interbacterial toxin delivery pathways. (a) The enzymatic reaction mechanism of papain-like cysteine proteases (PLCPs). The catalytic triad of residues in PLCPs, composed of cysteine (Cys), histidine (His), and aspartate (Asp), facilitates peptide bond cleavage. Histidine and aspartate form a proton-withdrawing group that activates the cysteine residue, converting it into a nucleophile. The activated cysteine attacks the carbonyl carbon of the peptide bond, leading to hydrolysis and bond cleavage. **(b)** Scaled depiction of representative genomic loci from the indicated species (*Edwardsiella tarda*, *Escherichia coli*, *Myxococcales bacterium*, *Roseofilum reptotaenium*, *Citrobacter rodentium*, *Rhizobium* sp., *Burkholderia* sp.) encoding predicted PLCP domain-containing proteins (sky blue) and putative cognate immunity proteins (yellow). Regions encoding N-terminal domains of T6SS-related proteins (PAAR, VgrG, Rhs) are shaded in gray. CDI-related proteins (CdiA, CdiB) are depicted in light brown. Black bars designate locations of bases encoding the catalytic triads of PLCPs. Cysteine residues targeted for mutagenesis in this study are depicted in red. **(c)** Sequence logo generated from alignments of PLCP domains associated with bacterial contact-dependent antagonism pathways (the locus tag numbers for genes encoding the sequences we used are provided in **Supplementary Table 1**). Sequences from previously characterized PLCPs ($ComA_{pep}$ and $LahT_{pep}$) and recently identified T6SS-associated PLCP toxins (EvpQ and TsaP) are shown below for reference. **(d)** Maximum likelihood phylogeny of PLCP effectors visualized as a radiating phylogenetic tree. Taxonomy is indicated by colored shadows, and delivery pathways are indicated by colored tips. The scale bar represents the average number of substitutions per site. See also **Supplementary Figure 2**.

Figure 2

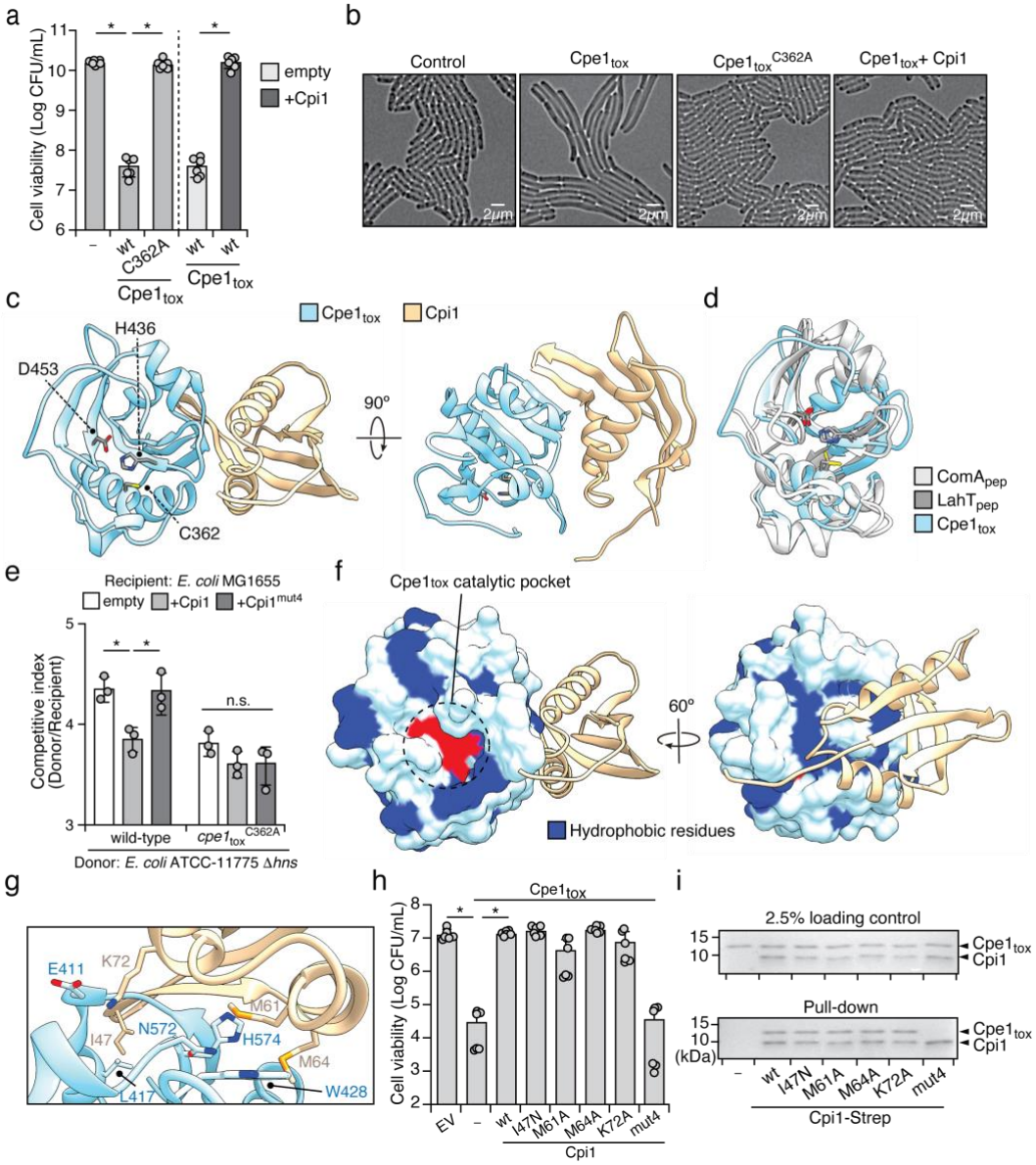

Figure 2. Cpe1$_{tox}$-Cpi1 is a functional effector-immunity pair. (a) Viable *E. coli* cells recovered from plating cultures carrying plasmids expressing the indicated proteins on inducing media. *E. coli* carrying plasmid-borne Cpi1 or an empty vector was included to validate suppression of Cpe1 toxicity. **(b)** Representative micrographs of *E. coli* cells expressing empty vector, Cpe1$_{tox}$, Cpe1$_{tox}^{C362A}$, or co-expressing Cpe1$_{tox}$ and Cpi1. Frames were acquired 2 hours after induction of protein expression. Scale bar, 2 μm. **(c)** Ribbon diagram representation of the X-ray crystal structure of Cpe1$_{tox}$ (sky blue) in complex with Cpi1 (light gold). Residues of the catalytic triad of Cpe1$_{tox}$ are indicated. **(d)** Structural alignments of Cpe1$_{tox}$ with previously characterized PLCPs: ComA$_{pep}$ (PDB: 3K8U, light gray) and LahT$_{pep}$ (PDB: 6MPZ, dark gray). **(e)** Bacterial competition experiments were conducted on a solid agar over a 6-hour period between the indicated donor and recipient strains. *E. coli* ATCC-11775 Δ*hns* served as the donor strain, whereas *E. coli* MG1655 was used as the recipient strain. The Δ*hns* mutation in the donor strain was introduced to upregulate T6SS activity, as described in previous studies[99-101]. **(f)** Depiction of Cpe1$_{tox}$ illustrating the Cpe1$_{tox}$-Cpi1 interaction at the exosite formed by hydrophobic residues. **(g)** Magnified view of the interface between Cpe1$_{tox}$ and Cpi1, highlighting the interacting residues on Cpi1 positioned near the hydrophobic concave surface of Cpe1$_{tox}$. **(h)** Viable *E. coli* cells recovered from *E. coli* co-expressing wild-type Cpe1$_{tox}$ and the indicated Cpi1 variants. **(i)** *In vitro* pull-down assay of Cpe1$_{tox}$ and Cpi1. Cpe1$_{tox}$ proteins were pulled down by strep-tagged Cpi1 variants and immobilized on streptavidin resin. Bound proteins were separated by SDS-PAGE followed by Coomassie brilliant blue staining. Data in **(a)**, **(e)**, and **(h)** are represented as means ± SD. Asterisks indicate significant differences ($p < 0.05$) in viability between populations **(a, h)** or statistically significant differences ($p < 0.05$) between competitive indices of a given donor strain toward the indicated recipients **(e)**. n.s. means no significance. See also **Supplementary Figure 3**, **Supplementary Table 2**, and **Videos 1-4**.

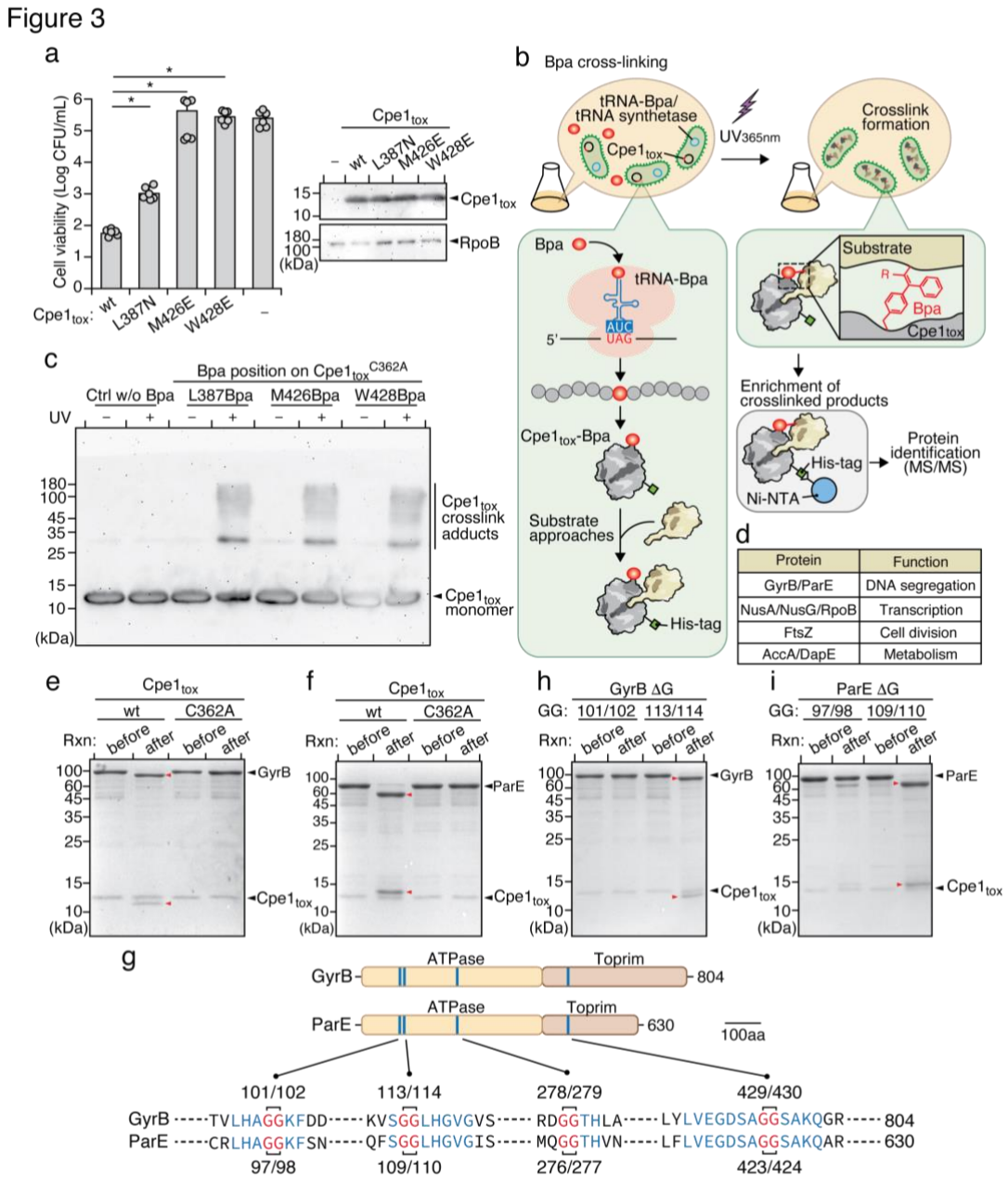

Figure 3. Cpe1$_{tox}$ targets and cleaves the type II DNA topoisomerases GyrB and ParE. (a) Viable *E. coli* cells recovered from expressing Cpe1$_{tox}$ with substitutions of indicated surface residues from the hydrophobic concave region. The expression levels of wild-type and Cpe1$_{tox}$ variants were assessed by immunoblotting analysis, using the cytosolic protein RpoB as a loading control (right panel). **(b)** Schematic workflow for identifying candidate substrates of Cpe1$_{tox}$ through Bpa crosslinking followed by LC-MS/MS protein identification. Bacteria carrying the construct with a TAG stop codon at residues of interest were grown in medium supplemented with Bpa. After incubation, cells were exposed to long-wavelength UV to activate formation of covalent bonds between Bpa and the interacting residues. Cell lysates were incubated with Ni-NTA resin to enrich for Cpe1$_{tox}$-Bpa crosslinks for further analysis. **(c)** SDS-PAGE gel analysis of crosslinked protein complexes before and after UV$_{365nm}$ treatment. Cpe1$_{tox}^{C362A}$-protein complexes enriched by the Ni-NTA resin were boiled in SDS sample buffer and separated by SDS-PAGE, followed by immunoblotting (α-His). **(d)** Essential proteins identified in the Cpe1$_{tox}^{C362A}$ interactome and their biological functions. The complete interactome dataset is available in **Supplementary Table 3**. **(e, f, h, i)** *In vitro* Cpe1$_{tox}$ cleavage assays. Purified Cpe1$_{tox}$ (wild-type or catalytic mutant) were incubated with purified candidate substrates, *i.e.,* GyrB **(e)** and ParE **(f)**, or their variants with single-glycine deletion at the predicted cleavage sites **(h, i)**, to assess hydrolysis by Cpe1$_{tox}$. Fragmented proteins are marked with red arrowheads. Rxn means reaction. **(g)** Double glycine motifs in the consensus regions of *E. coli* GyrB and ParE. Locations of consensus regions between GyrB and ParE containing double glycine motifs are indicated on the cartoon representation of the full-length proteins. The sequences of the consensus regions are shown below, with the positions of the double glycine motifs labeled. The GG motif (red) and the surrounding residues (blue) are highlighted.

Figure 4

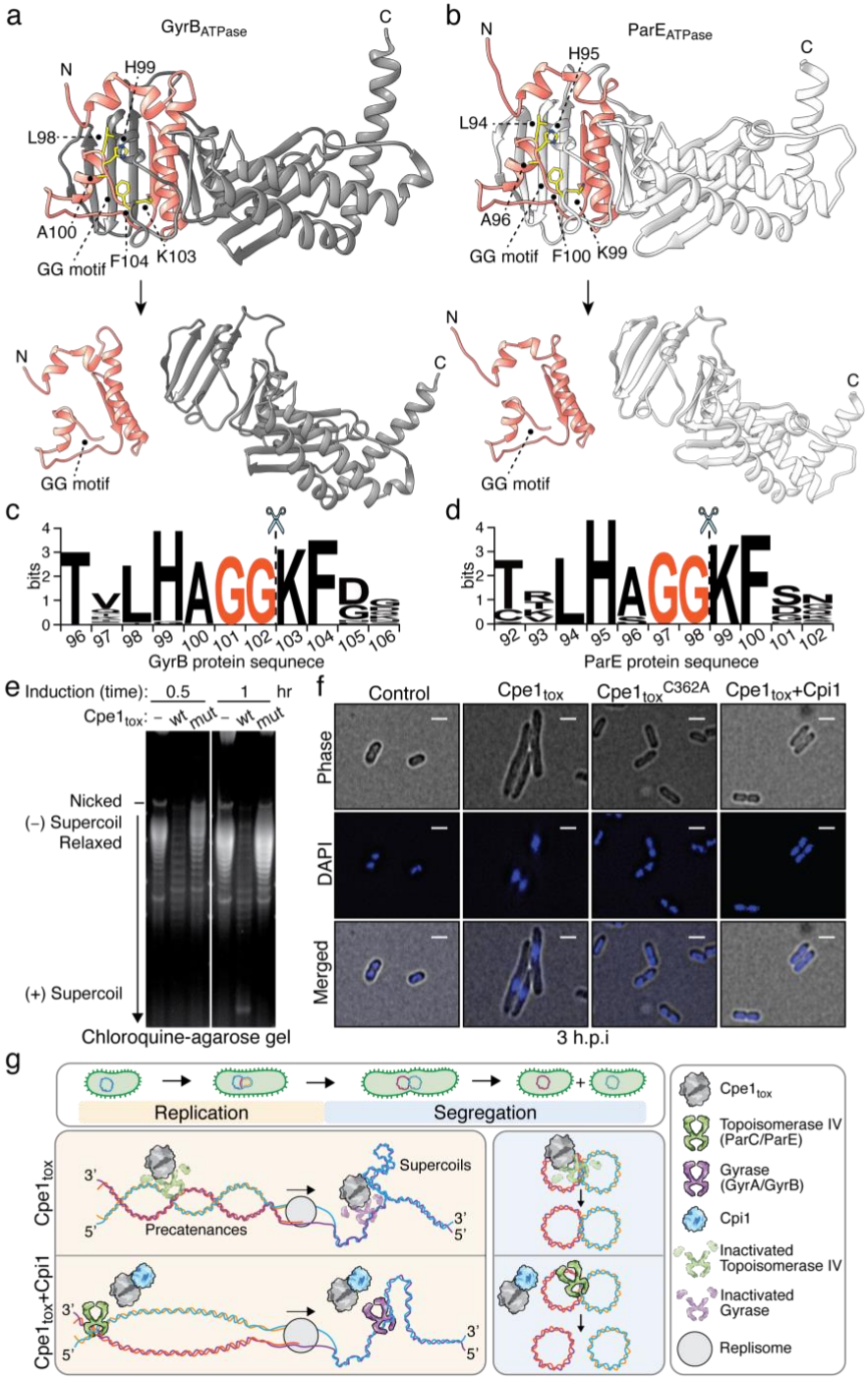

Figure 4. Cpe1$_{tox}$-mediated intoxication disrupts topoisomerase activity, thereby altering DNA topology and impairing DNA replication and chromosome segregation. (a-b) Ribbon diagrams of *E. coli* GyrB (a, top structure) and ParE (b, top structure) before and after cleavage by Cpe1$_{tox}$. Crystal structures of the 43-kDa ATPase domain of *E. coli* GyrB (PDB: 4PRV) and ParE (PDB: 1S16) were used. Residues of the consensus sequence (LHAGGKF) are shown in yellow. Structure related to the small fragments after Cpe1$_{tox}$ cleavage are indicated as pink ribbons. Predicted structures after cleavage at the double glycine motif demonstrated disruption of the ATPase domain of both GyrB (a, bottom structure) and ParE (b, bottom structure). **(c, d)** Sequence logos evidencing conservation of the consensus sequence (LHAGGKF) of GyrB **(c)** and ParE **(d)** homologs. Cleavage at the double glycine motif is indicated by dashed lines and a scissors illustration. **(e)** Plasmid DNA (pET) was analyzed by high-resolution agarose gel electrophoresis following isolation from *E. coli* that had expressed Cpe1$_{tox}$ or the catalytic mutant for 0.5 or 1 hour. **(f)** *E. coli* cells that had expressed Cpe1$_{tox}$, Cpe1$_{tox}^{C362A}$, or Cpe1$_{tox}$ co-expressed with Cpi1 for three hours. Cpe1$_{tox}$, or the catalytic mutant, was stained with DAPI (DNA; blue) and analyzed by fluorescence microscopy. Phase-contrast (top), blue fluorescence (middle), and merged (bottom) images are presented. Scale bar = 2 µm. Full-size images are available in **Supplementary Figure 7**. **(g)** Working model of how Cpe1 intoxicates bacteria. During interbacterial competition, Cpe1 targets and cleaves the ATPase domains of GyrB and ParE in target cells. The cleavage leads to accumulations of unrelaxed supercoils and precatenanes, disrupts DNA segregation, and ultimately inhibits cell division and growth. In the Cpe1-producing cells or kin cells expressing the immunity protein Cpi1, Cpe1 toxicity is neutralized through direct interaction between Cpe1 and Cpi1.

Figure 5

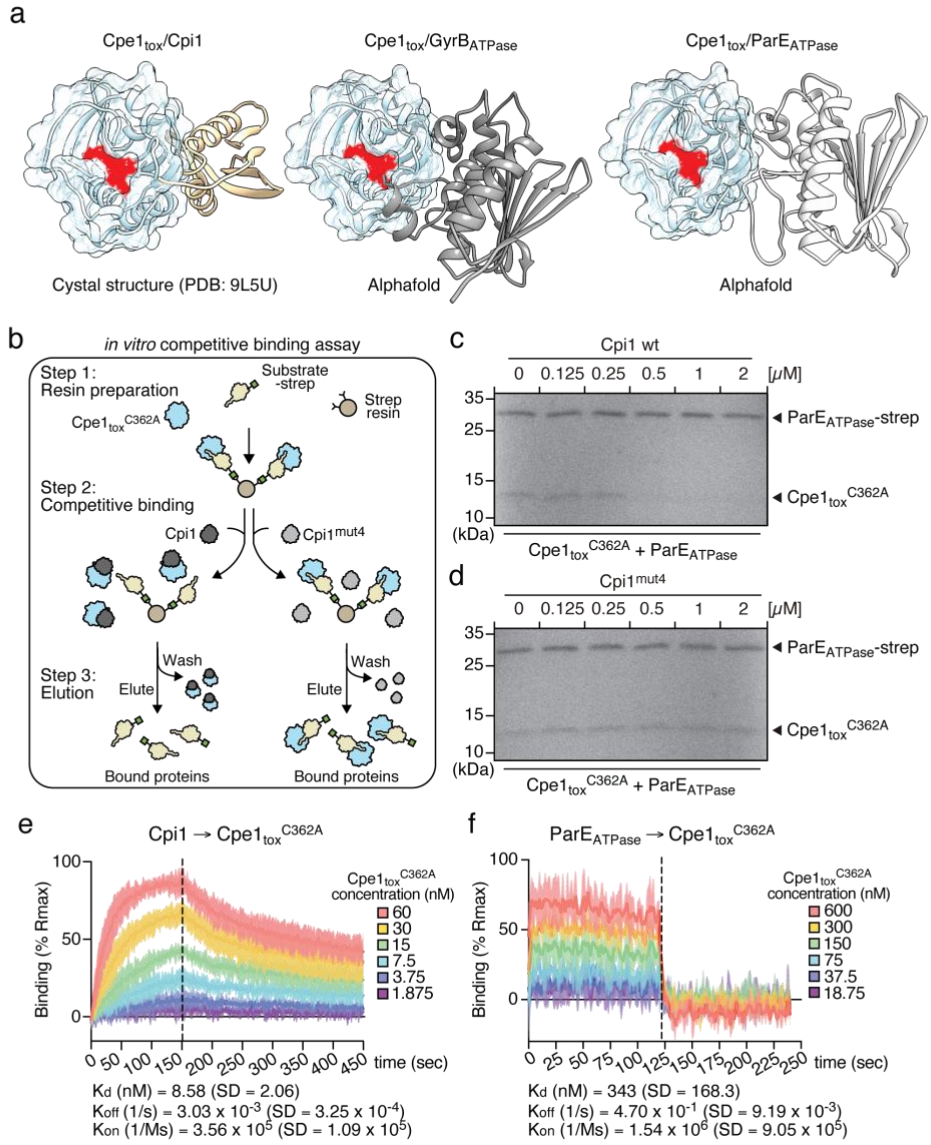

Figure 5. Cpi1 employs a competitive inhibitory mechanism to neutralize Cpe1. (a) The $Cpe1_{tox}$-Cpi1 interface overlaps with the $Cpe1_{tox}$-substrate interaction site. Model predictions of interaction between $Cpe1_{tox}$ and the ATPase domains of GyrB and ParE were constructed using AlphaFold 3. See also **Supplementary Figures 9a, b** for confidence metrics. **(b)** Schematic workflow for the *in vitro* competitive binding assay. Streptavidin resins bound to pre-formed $Cpe1_{tox}^{C362A}$-substrate complexes were prepared and incubated with either wild-type or mutant Cpi1. After incubation, the resins were washed, and the bound proteins were eluted for analysis. Competitive binding events are indicated by disruption of the $Cpe1_{tox}^{C362A}$-substrate interaction, leading to a decreased level of $Cpe1_{tox}^{C362A}$ in the eluted fraction due to its removal during the wash step. **(c, d)** Coomassie-stained SDS-PAGE demonstrating competitive binding events. **(e, f)** Kinetic analysis of interactions between Cpi1 and $Cpe1_{tox}^{C362A}$ **(e)** and $ParE_{ATPase}$ and $Cpe1_{tox}^{C362A}$ **(f)** using biolayer interferometry (BLI). Data from three replicates have been plotted on an X-Y scatter graph. The Y-axis represents the wavelength shift generated by binding of the two proteins, normalized to the calculated Rmax (% Rmax) for each run. The X-axis represents reaction time (in seconds). A vertical dashed line marks the transition from the association step to the dissociation step. The mean kinetic parameters (K_d, K_{on}, and K_{off}) and their standard deviations are indicated.